



Rationally designed oxygen vacant TiO_2 decorated with covalent organic framework for enhanced electrocatalytic nitrogen reduction to ammonia

Biswajit Mishra^a, Swayamprakash Biswal^a, Mohd. Ussama^b, M. Ali Haider^b, Bijay P. Tripathi^{a,*}

^a Functional Materials and Membranes Laboratory, Department of Materials Science & Engineering, Indian Institute of Technology Delhi, New Delhi, 110016, India

^b Renewable Energy and Chemicals Laboratory, Department of Chemical Engineering, Indian Institute of Technology Delhi, Hauz Khas, New Delhi, 110016, India

ARTICLE INFO

Keywords:

Covalent organic framework
Anthraquinone
Oxygen vacant TiO_2
Noble metal-free catalyst
Electrocatalytic nitrogen reduction

ABSTRACT

This study focuses on the rational design of uniformly distributed oxygen vacant TiO_{2-x} nanoparticles supported on an anthraquinone-based covalent organic framework (TiO_{2-x} @COF-Aq), aiming to address the challenges of Haber-Bosch process. The N-philic nature of Ti and the presence of abundant oxygen vacant sites on the TiO_{2-x} @COF-Aq promote the adsorption of nitrogen, facilitating the electrocatalytic NRR process. The theoretical study reveals that TiO_{2-x} @COF-Aq suppresses the H^+ adsorption, facilitates oxygen vacancy formation and favors the N_2 adsorption at oxygen vacant sites. The synthesized nanocatalyst exhibits many folds higher electrochemical NRR activity than bulk oxygen vacant TiO_{2-x} with an ammonia yield of $\sim 30 \mu\text{g mg}^{-1} \text{h}^{-1}$ and $\sim 16\%$ Faradaic efficiency. Long term stability study manifests the robustness and industrial significance of the catalyst. The overall synergism between the stabilized nanoparticle and functionalized COF has established the fundamental understanding of the proton coupled electron transfer for N_2 fixation through experiments and theoretical findings.

1. Introduction

Ammonia having a large weight percentage of hydrogen ($\sim 17.7\%$), provides a sustainable alternative to a carbon-free energy sources [1,2]. The ease of breaking it down to yield high-purity hydrogen and its ability to liquefy at ambient temperature and moderate pressure conditions have significantly increased the industrial production of ammonia [3,4]. However, the bottleneck issue lies in the traditional route of ammonia production through the Haber-Bosch process, which operates at elevated temperature and pressure ($300\text{--}500^\circ\text{C}$, $200\text{--}500$ bar) [5]. The high inertness and bond dissociation energy of $\text{N}\equiv\text{N}$ molecules (940.95 kJ/mol) require these harsh reaction conditions for ammonia production [6]. Based on an annual estimation report, approximately 2% of global energy consumption and over 450 million tons of CO_2 emission are attributed to Haber-Bosch process for commercial ammonia synthesis [1,7]. However, the electrochemical nitrogen reduction reaction (ENRR) has recently gained considerable attention as a potential alternative, as it utilizes inexpensive electrocatalysts and operates under ambient reaction conditions to convert N_2 molecules into ammonia [4,8]. The development of a suitable ENRR catalyst relies on its ability to facilitate electron transfer between the

catalyst surface and the adsorbed N_2 molecule by reducing the charge transfer barrier. Additionally, the choice of electrolyte plays a crucial role in the electrolysis process, as the formation of ammonia involves both electron and proton transfer. In recent past, researchers have reported several catalysts, including noble metal-based catalysts, metal oxide, metal sulfides, and metal nitrides. However, many of these reported catalysts suffer from significant limitations like poor Faradaic Efficiency ($\text{FE} \approx 10\%$) and low ammonia yield, restricting their industrial utility [9]. These lower catalytic performances are often associated with poor catalyst stability in the electrolyte medium, selectivity issues with competitive cathodic reactions like hydrogen evolution reaction (HER), and elevated charge transfer barriers for the proton coupled electron transfer (PCET) mechanism for $\text{N}\equiv\text{N}$ cleavage [10]. To overcome these drawbacks of ENRR, catalyst materials with engineered band gaps should be prepared with modified d-band centers to facilitate ENRR activity [11].

Density functional theory (DFT) simulations have revealed that metal centers in low valence states tend to amplify the electron donation ability to the antibonding orbitals of N_2 molecules, leading to the weakening and dissociation of N_2 molecules to form NH_3 [12,13]. Most recent reports have shown that noble metal-based (Ru, Au, etc.) catalysts

* Corresponding author.

E-mail addresses: bptripathi@mse.iitd.ac.in, drbptripathi@gmail.com (B.P. Tripathi).

<https://doi.org/10.1016/j.apcatb.2023.123395>

Received 28 June 2023; Received in revised form 25 September 2023; Accepted 11 October 2023

Available online 13 October 2023

0926-3373/© 2023 Elsevier B.V. All rights reserved.

exhibit better ENRR activity due to their strong adsorption tendency towards N_2 and intermediates [14]. However, the scarcity, high cost, and ease of H-adsorption limit their usage in various industrial applications. For instance, Pt and Ir-based catalysts preferentially adsorb H over N_2 , resulting in enhanced HER activity compared to NRR due to their strong tendency to form M-H bonds [15]. On the other hand, transition metal oxides, carbides, and nitrides, which are cheaper and abundantly available, have been explored as electrocatalysts by modifying their structure with vacancies, defects, interfaces, etc. Among various such systems, theoretical studies have revealed that the Ti center is favorable for binding N_2 molecules over H and the reactant intermediates on its empty d-band, thereby facilitating the overall NRR activity [16–18]. However, their practical applicability is hindered by low NH_3 yield and FE due to slow reaction kinetics and moderate selectivity. Therefore, it is crucial to redesign TiO_2 by modulating the overall electronic environment and rationally tuning the active center to enhance NRR activity.

Defect modulation in metal oxides can significantly increase catalytic activity by reducing the adsorption energy of intermediates, energy barrier for transition states, and stabilize metal atoms at the atomic level. Oxygen vacancies in TiO_2 , for example, have been shown to promote N_2 adsorption through their vacant sites, providing electrons to N_2 antibonding orbitals, and facilitating the adsorption and reduction of N_2 molecules to ammonia. Hirakawa and co-workers have demonstrated enhanced NRR performance on TiO_2 based catalysts and limiting the HER reactivity of the surface [19]. Defect sites are expected to further improve the interaction of N_2 with the TiO_2 surface, as proposed by Walter and co-workers [20]. Recent studies emphasize the crucial role of oxygen vacant TiO_2 in enhancing ENRR and other electrocatalytic applications. Chen et al. reported Ru nanoparticles supported on an oxygen vacant TiO_2 surface and observed improved ENRR activity with the Ru/TiO_2-V_o due to the presence of oxygen vacant TiO_2 sites [21]. A thorough understanding of the role of oxygen vacancy on TiO_2 to promote the ENRR using both theoretical calculations and experimental observations was explored by Han et al. [22]. Li et al. observed that TiO_2 with oxygen vacant sites facilitate the chemisorption and activate N_2 molecules, thereby enhancing the overall ENRR activity [23]. Due to these characteristics, a variety of methods have been developed for synthesizing oxygen vacant TiO_2 for a wide range of applications. Aside from multiple experimental processes, the reported oxygen vacant TiO_2/Ti^{+3} catalyst displays lower NRR activity because of its lower oxygen vacant TiO_2 concentration, lower active centers, and higher work function. Since NRR is a multi-step reaction involving a six-electron and proton transfer process to produce ammonia, it is crucial for a catalyst to have a higher number of active centers and lower work function to overcome the kinetic barrier. This can be achieved by creating adequate adsorption sites for N_2 and reactant intermediates and facilitating faster electron transfer rates to promote the reduction process.

Recent studies have revealed that nanosized particles provide abundant active sites that significantly enhance catalytic activity compared to their bulk counterparts. For instance, Wu and coworkers investigated the effect of size of Mo nanoparticles on electrochemical NH_3 synthesis and observed that smaller Mo nanoparticles (~1.5 nm) exhibited superior ENRR activity compared to larger sized particles. A comprehensive understanding from the DFT analysis affirmed that the smaller-sized particles provide more exposed edge sites between (110) and (100) surfaces, thereby providing sufficient binding sites for N_2 adsorption, thus facilitating the ENRR process [24]. Similarly, Feng et al. synthesized Ru nanoparticles of varying sizes, ranging from 2.1 to 8.4 nm, and found that Ru nanoparticles with a size of 3.8 nm displayed superior ENRR activity compared to those with a size of 8.4 nm. DFT analysis revealed that the Ru nanoparticles of ~4 nm provided sufficient binding sites for ENRR activation and strengthens the intermediates to facilitate the ENRR process [25]. These investigations have affirmed the pivotal influence of nanoparticle size on ENRR activity. However, it is

worth noting that downsizing often leads to increased surface energy, which can result in particle agglomeration and Ostwald ripening.

To address this problem, nanoparticles are often prepared on suitable substrates (e.g., 2-D materials), which provide a strong metal-support interaction and facile electron transfer at the interface. 2-D materials with higher surface area and uncoordinated surface atoms are advantageous for catalytic reactions as they readily provide uniformly distributed small-sized nanoparticles as catalytically active centers. Unlike graphene, covalent organic frameworks (COFs) represents a class of crystalline porous materials with higher surface area, abundant functional sites, and a symmetrical porous architecture that can provide sufficient nucleation sites to anchor nanoparticles [26]. Furthermore, for long-term applicability of an electrocatalyst, enhancing its stability is of paramount importance, which can be achieved through the establishment of a strong metal-support interaction (SMSI) [27]. In this context, COFs due to their higher surface area and adequate functional sites are often chosen as support materials to stabilize nanoparticles through SMSI [28]. Importantly, SMSI not only prevents the aggregation of nanoparticles but also facilitates the electron transfer process between the catalyst and intermediates, thereby enhancing overall electrocatalytic activity [29].

In this context, we have successfully synthesized nanosized oxygen vacant TiO_2 (TiO_{2-x}) on a conductive 2-D anthraquinone-based COF (COF-Aq) support using a hydrothermal-calcination approach. The oxygen vacant TiO_{2-x} nanoparticles have been uniformly distributed throughout the COF-Aq, with a narrow particle size distribution of 7 ± 2 nm. COF-Aq, having a higher surface area (~1180 m²/g) with adequate functional sites, provides numerous nucleating sites to anchor and stabilize the TiO_{2-x} nanoparticles. XPS and EPR analysis have confirmed a significantly higher concentration of oxygen vacancies in $TiO_{2-x}@COF-Aq$ compared to bulk TiO_{2-x} . Benefiting from the synergetic effect arising from TiO_{2-x} and COF-Aq, the designed electrocatalyst exhibits impressive performance in ammonia synthesis. At -0.5 V vs. RHE, the $TiO_{2-x}@COF-Aq$ electrocatalyst achieves a high ammonia yield rate of approximately 30 $\mu g h^{-1} mg^{-1}$ with a Faradaic efficiency of 16%. These values are substantially higher than those of bulk oxygen vacant TiO_{2-x} and many reported noble metal-based catalysts. Mechanistic investigations have revealed that $TiO_{2-x}@COF-Aq$ exhibits a higher affinity for N_2 adsorption, lower charge-transfer resistance, and a lower work function leading to enhanced ENRR activity compared to bulk TiO_{2-x} . Furthermore, $TiO_{2-x}@COF-Aq$ demonstrates reduced energetics for oxygen vacancy formation on its surface compared to pure TiO_{2-x} , thereby facilitating the formation of oxygen vacancies within $TiO_{2-x}@COF-Aq$. The presence of oxygen vacancies on the $TiO_{2-x}@COF-Aq$ facilitates the N_2 adsorption with an energy of -108 kJ/mol, surpassing the energy of the H-adsorption (-67 kJ/mol), resulting in a preferential activation of N_2 and NRR activity. Moreover, under prolonged ENRR activity test for up to 60 hr, the catalyst showed consistent performance without any noticeable structural and morphological deterioration. This provides strong evidence for the industrial applicability of the $TiO_{2-x}@COF-Aq$ catalyst.

2. Experimental sections

2.1. Synthesis of 1,3,5-triformylphloroglucinol (TFP)

1,3,5-triformylphloroglucinol was synthesized according to the literature procedure [30]. Briefly, hexamethylenetetramine (5.033 g, 36 mmol) and dried phloroglucinol (2.004 g, 16.33 mmol) were added in a round bottom flask under N_2 atmosphere. Thereafter, 30 mL of tri-fluoroacetic acid was added to this mixture and heated at 100 °C for 2.5 h under constant stirring. After that, approximately 100 mL of 3 M HCl was added to the above solution and heated at 100 °C for another 1 h. The solution was then cooled to room temperature, followed by filtration and extraction with ca. 250 mL dichloromethane. The obtained organic layer was dried over anhydrous magnesium sulphate overnight.

Rotary evaporation of the solution resulted in an orange powder, which was further dissolved in DCM followed by repeated washing with 1 M HCl and deionized water to remove any remaining trace impurities. The final product was obtained as an off-white powder.

Yield-18.6%, ^1H NMR (400 MHz, CDCl_3 , Fig. S1) δ 14.11 (s, 3 H, OH), 10.15 (s, 3 H, CHO) ppm; ^{13}C NMR (400 MHz, CDCl_3 , Fig. S1) δ 191.04 (CHO), 172.58 (C–OH), 102.9 (C–CHO) ppm; FT-IR (cm^{-1}) peaks at 2922, 1645, 1604, 1428, 1388, 1258, 1184, 946, 858, 606].

2.2. Synthesis of COF-Aq

Anthraquinone based COF was synthesized using the previously reported method by DeBlase et al. [31]. DAAQ (102 mg, 0.426 mmol) and TFP (60 mg, 0.288 mmol) was mixed in dimethylacetamide (3 mL) in a glass tube. The resulting suspension was sonicated for 60 s, and a 150 μL acetic acid (6 M) was added, and the whole mixture was further sonicated for about 10 min. After that, the mixture was degassed using three consecutive freeze-pump-thaw cycles and placed in an oven at 90 $^\circ\text{C}$ for two days. The resulting COFs were collected by centrifugation and repeated washing with DMAc and water. Finally, the collected solid was dried at 90 $^\circ\text{C}$ under vacuum for 24 h.

2.3. Synthesis of self-doped TiO_{2-x} @COF-Aq

Self-doped TiO_{2-x} on COF-Aq support was synthesized using a modified hydrothermal-calcination method [32]. 50 mg of COF-Aq was dispersed into a 10 mL of isopropyl alcohol/water mixture (1:4 ratio) and sonicated for ca. 3 min. After sonication, 1.5 mL nitric acid (0.1 M) was added and mixed vigorously for 5 min. To the above mixture, 250 μL of titanium isopropoxide was added, and further sonicated for ca. 15 min. The color of the mixture turns from deep red to light red. Thereafter, the suspension was transferred to an autoclave (Techinstro, India) and heated at 180 $^\circ\text{C}$ for 18 h. The final TiO_{2-x} @COF-Aq was recovered by filtration and repeated washing with water and ethanol followed by drying under vacuum. The final residue was calcined at 180 $^\circ\text{C}$ under N_2 atmosphere with a ramp rate 1 $^\circ\text{C}/\text{min}$. Similarly, oxygen vacant TiO_{2-x} was prepared by keeping similar concentration of reactant without using COF-Aq in the reaction mixture. To compare the effect of oxygen vacancy on the ENRR activity, TiO_2 nanoparticle without oxygen vacancy was designed over COF-Aq using similar protocol without calcination under N_2 atmosphere and designated as TiO_2 @COF-Aq.

2.4. Material characterizations

The FT-IR spectra of synthesized monomer, COF, and TiO_{2-x} @COF-Aq were recorded using KBr pellet method on a Nicolet IR 6700 spectrometer (ThermoFischer scientific, USA). Thermogravimetric analysis (TGA) was performed using the Pyris-6 thermogravimetric analyzer (PerkinElmer, USA) instrument at a heating rate of 10 $^\circ\text{C}/\text{min}$ under an N_2 environment. Powder wide-angle X-ray diffraction (PXRD) pattern of COF-Aq and TiO_{2-x} @COF-Aq was recorded on a Rigaku, Ultima IV diffractometer with a $\text{Cu K}\alpha$ X-ray source ($\lambda = 1.54 \text{ \AA}$). The diffraction pattern was collected using a continuous 2θ scan from 2 to 80 $^\circ$ with a scan speed of 1 $^\circ/\text{min}$ (step size 0.01 $^\circ$). The structural refinement using the Rietveld method was carried out using the MAUD program. The morphological attributes were obtained using transmission electron microscopy (TEM; JEM-1400, JEOL) and field emission scanning transmission electron microscopy (FESEM; JSM-7800 F Prime, JEOL). High-resolution transmission electron microscopy (HRTEM) images were obtained by a Tecnai G2 F20 S-TWIN electron microscope. The chemical state of elements and synthesis of TiO_2 nanoparticles on the surface on COF-Aq were confirmed with a PHI 5000 VersaProbe III X-ray photoelectron spectrophotometer (Physical Electronics) using a monochromatic Al $\text{K}\alpha$ X-ray source. All samples were stored in a vacuum for 24 h prior to analysis. The N_2 adsorption/desorption isotherms were obtained using Autosorb-iQ XR (Quantachrome Instruments). Nitrogen

isotherm was generated using 40–40 points at 77 K (using liquid N_2) for 24 h. The UV–visible spectra of the powder sample were recorded using UV-3600i plus spectrophotometer (Shimadzu, Japan) using External 3 Detector mode. Initially, the powder sample was loaded on the sample holder, and the transmittance value was recorded. Absorbance values were calculated by LabSolutions UV–vis software using the Kubelka-Munk equation. The electron paramagnetic resonance (EPR) measurements were done using powder sample at room temperature, and the spectra were recorded JES-FA200 ESR Spectrometer (JEOL, Japan) equipped with X-band (8.75–9.65 GHz). Nitrogen temperature-programmed desorption (N_2 -TPD) profiles of the electrocatalysts were measured using a BELCAT II chemisorption catalyst analyzer (MicrotracBEL Corp). Prior to analysis the sample was degassed for 1 h at 100 $^\circ\text{C}$, followed by cooled down to 50 $^\circ\text{C}$. After that, high purity N_2 gas was continuously purged to the chamber at 50 $^\circ\text{C}$ for 2 hr. Subsequently, after purging with Helium gas for 1 hr, the desorption profiles were recorded from 50 $^\circ$ to 500 $^\circ\text{C}$ with a 10 $^\circ\text{C}/\text{min}$ ramp rate. Raman analysis was conducted within a spectral range between 300 and 100 cm^{-1} using a Micro Raman spectrometer (Renishaw plc, UK) equipped with an Ar laser source (514 nm).

2.5. Electrocatalytic nitrogen reduction reaction (ENRR)

ENRR was performed using a H-type cell separated by a proton membrane under room temperature and atmospheric pressure. Prior to electrocatalysis, the Nafion membrane was activated in 5 wt% H_2O_2 solution at 50 $^\circ\text{C}$ for 1 h followed by washing with deionized water. After that, the membrane was kept in 0.1 M HCl for 12 hr and finally the membrane was repeatedly washed with DI water and stored in DI water at room temperature. High-purity N_2 gas was purchased from Sigma gases and passed to the electrolyte after confirming the absence of trace NH_3 and NO_x . Electrochemical measurements were conducted with a Autolab M204 potentiostat (Metrohm) using a standard three electrode system using a catalyst loaded-glassy carbon (3 mm) as working electrode, a saturated Ag/AgCl (in 3 M KCl) as the reference electrode, and a platinum plate as counter electrode. The catalyst slurry was prepared by dispersing 1 mg of catalyst 1.4 mL of DMF: H_2O (4:1) and 40 μL of Nafion solution. The solution was thoroughly sonicated for 1 hr at room temperature to get the catalyst slurry. Finally, 10 μL of slurry was drop-casted on the glassy carbon surface (catalyst loading 0.1 mg/cm^2). The catalyst was kept undisturbed and dried at room temperature (Note: the catalyst layer should smooth, and no crack was observed after drying). For the long-term stability, the catalyst was mounted on a Torey carbon paper by keeping similar catalyst loading (0.1 mg/cm^2). All the potential reported in the work are converted from Ag/AgCl to RHE scale via using following equation, $E \text{ (vs RHE)} = E \text{ (vs Ag/AgCl)} + 0.197 + 0.059 \times \text{pH}$. Linear sweep voltammograms (LSV) measurements were performed using 0.1 M HCl with a scan rate of 5 mV sec^{-1} . Prior to performing the N_2 reduction reaction, the electrolyte was purged with N_2 using Metrohm-made cell gas purge apparatus for 30 min (flow rate 50 mL/min) to obtain a saturated concentration of dissolved N_2 . In order to avoid the volatilization of ammonia, another cell was fitted at the end of the cathodic compartment, filled with 20 mL of 0.1 M HCl as the NH_3 absorption liquid. After ENRR, the cathodic electrolyte along with the absorption liquid were both collected, mixed, and analyzed for quantifying the ammonia production. During the measurement, N_2 gas was continuously bubbled at a flow rate of 50 mL/min , the corresponding chronoamperometry results were recorded at different potential. For long-term ENRR stability, chronoamperometry was performed using catalyst mounted over a Torey carbon paper. More detailed explanation about the ENRR measurements is available in the [Supporting Information \(Section S2\)](#).

2.6. Computational methods and models

The energy and structure optimization are performed using DFT

calculations, as implemented in the CP2K code of QUICKSTEP module with a mixed Gaussian and plane-wave basis sets [33,34]. The electron interactions are described using the generalized gradient approximation for the exchange-correlation functional as proposed by Perdew, Burke, and Ernzerhof [35]. The Hubbard's parameter (U) for the DFT+U correction is set as 3 eV for Ti [36]. Core electrons are treated with norm-conserving Goedecker–Teter–Hutter pseudopotentials, and the valence electron wavefunctions are expanded in double zeta basis sets [37,38]. The kinetic energy cut-off was set to 400 Ry and the SCF convergence criterion is 1.0×10^{-8} a.u. with the maximum force convergence criteria of 0.001 Hartree/Bohr. In order to include the Van der Waals interactions, Grimme DFT-D3 interactions are included in all calculations [39]. The anatase TiO_2 (101) surface is modelled as a periodic slab with the vacuum layer of 15 Å in the z-direction. During structural optimizations, all atoms except those in the bottom layer of the TiO_2 slab are allowed to relax. The adsorption energy of X species (E_{ad}^{X}) is defined as the energy difference before and after the adsorption as,

$$E_{\text{ad}}^{\text{X}} = E(\text{total}) - E(\text{surface}) - E(\text{X})$$

where $E(\text{surface})$, $E(\text{X})$, and $E(\text{total})$ are the energies for the clean surface, X species in the gas phase, and X species adsorbed on the surface, respectively.

The Oxygen vacancy formation energy are calculated using the below relation,

$$E(\text{Ovac}) = E_{\text{Ovac_Complex}} + \frac{1}{2} E_{\text{O}_2(\text{g})} - E_{\text{Complex}}$$

where E_{Complex} is the energy of the complex without oxygen vacancy, $E_{\text{O_Vac_Complex}}$ is the energy of the complex with oxygen vacancy, and $E_{\text{O}_2(\text{g})}$ is the energy of the oxygen molecule in gas phase. In order to compare the NRR and HER activity, models representing TiO_2 in both the surface and nanocluster forms are introduced. Stable TiO_2 nanocluster with the molecular formula of $(\text{TiO}_2)_4$ proposed by Francesc and co-workers [40] is taken and mounted on the COF. DFT simulation are performed to study nitrogen and hydrogen adsorption on both the systems [33]. Charge analysis of adsorbed structure is performed using the restrained electrostatic potential (RESP) fit charge model as available in the Cp2k code [41].

3. Result and discussion

3.1. Synthesis of COF-Aq and $\text{TiO}_{2-x}\text{@COF-Aq}$

A schematic representation of the synthesis of COF and its modification with TiO_2 nanoparticles is shown in Fig. 1. The β -ketoenamine linked 2D COF-Aq was synthesized using Schiff-base condensation of 1,3,5-triformylphloroglucinol (TFP) and 2,6-diaminoanthraquinone (DAAQ) in the presence of 6 M acetic acid in DMAc. The resulting red colored powdered material with a yield of 84.3% was isolated as COF-Aq and was subsequently utilized as a substrate for synthesizing TiO_2 nanoparticles. The light red colored TiO_2 nanoparticle functionalized COF-Aq was prepared by a single-step reaction of COF-Aq with titanium isopropoxide in a mild acidic medium using hydrothermal-calcination approach. The higher surface area and defect sites on COF-Aq can provide a higher number of nucleation sites for anchoring ultrafine oxygen deficient TiO_{2-x} .

3.2. Characterization of materials

The morphology of the COF-Aq and $\text{TiO}_{2-x}\text{@COF-Aq}$ was analyzed using field emission scanning electron microscopy (FESEM) and high-resolution transmission electron microscopy (HRTEM). FESEM images (shown in Fig. S2, Supp. Info.) revealed a flake-like morphology of COF-Aq, which remained intact after the TiO_{2-x} nanoparticle formation, confirming the robust nature of COF-Aq. The low magnification TEM images shown in Fig. S2C (Supp. Info.) confirm the sheet-like layered build-up of COF-Aq, resulting from the stacking of layered macromolecules due to strong π - π interaction. As shown in the Fig. 2, the TiO_{2-x} nanoparticles were well-distributed throughout the COF-Aq support, with an average particle size of 7 ± 2 nm. The presence of nanoparticles on the COF-Aq surface suggests that the particle size might be larger than the pore size of the COF matrix. Additionally, it is also expected that some particles with a diameter of less than 2 nm move into the interplane of COF sheets, resulting in a decreased surface area. This assumption was further supported by N_2 adsorption/desorption isotherms. Fig. 2(E) represents the selected area electron diffraction (SAED) pattern of TiO_2 , indicating the crystalline nature of the $\text{TiO}_{2-x}\text{@COF-Aq}$

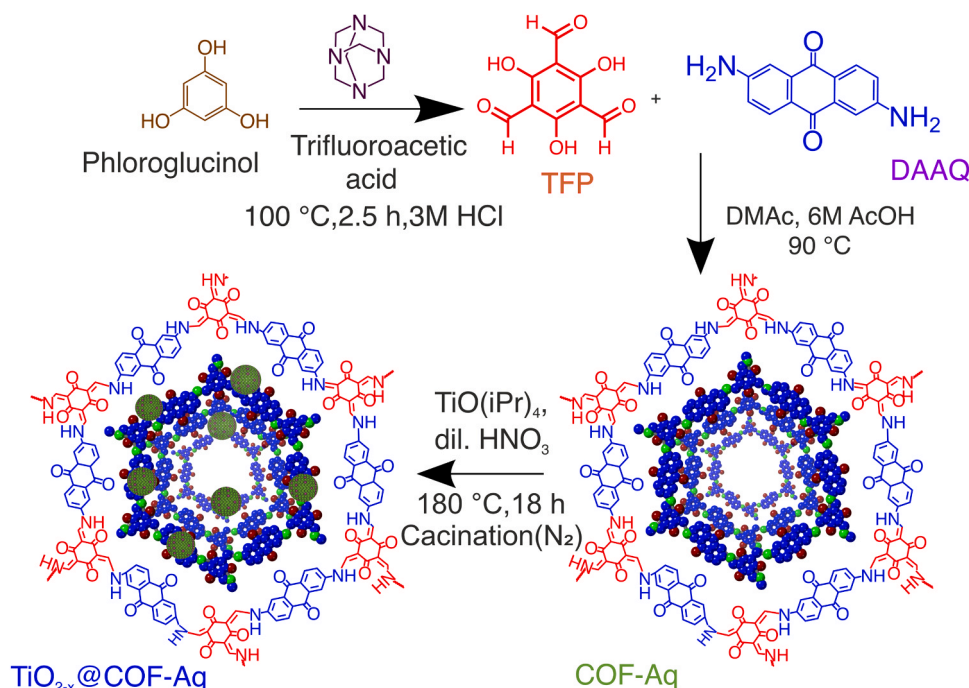


Fig. 1. Stepwise schematic illustration for the synthesis of 1,3,5-triformylphloroglucinol, formation of COF-Aq, and $\text{TiO}_{2-x}\text{@COF-Aq}$ in presence of dilute HNO_3 .

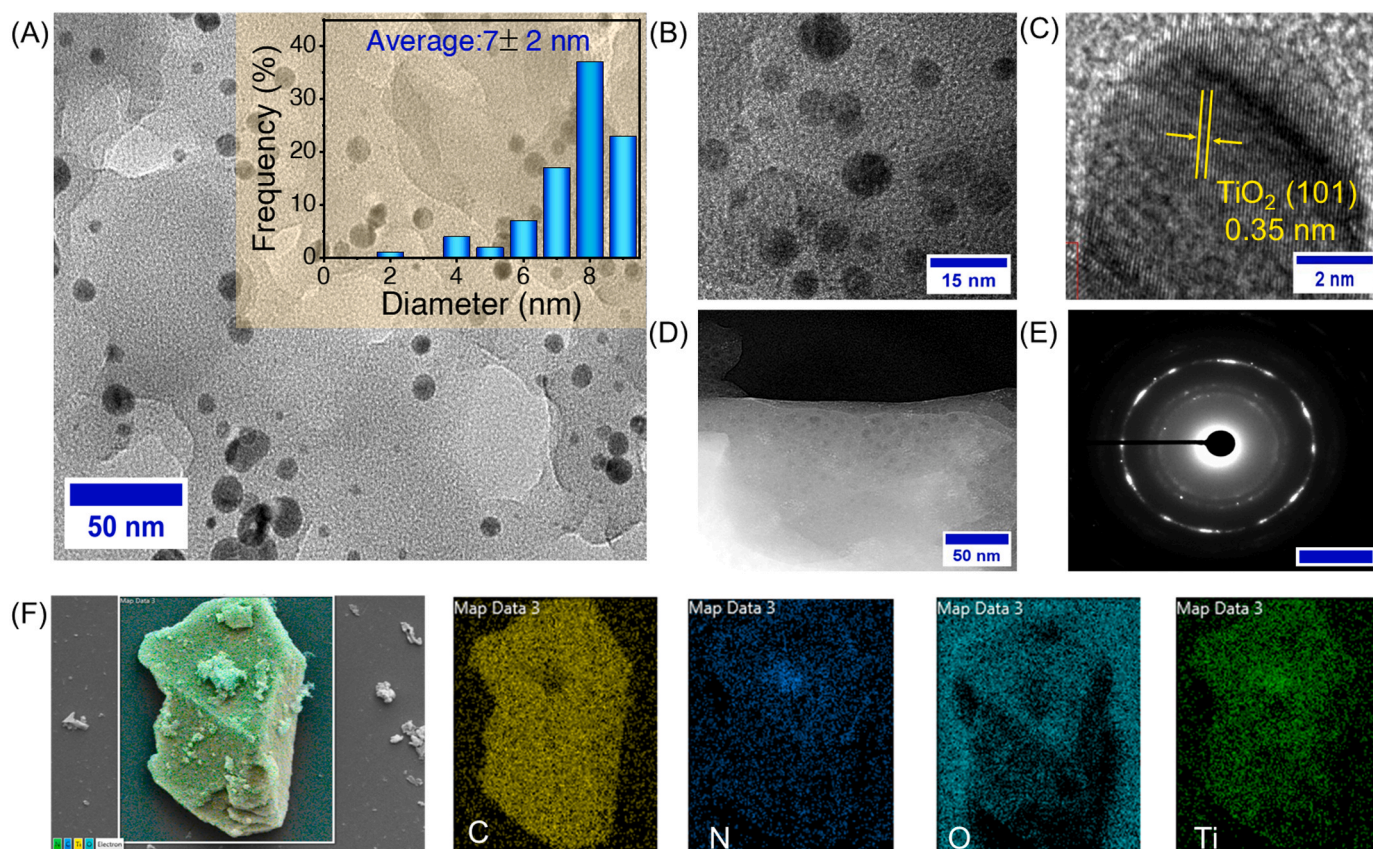


Fig. 2. (A) Low magnification bright-field HRTEM image of $\text{TiO}_{2-x}\text{@COF-Aq}$ showing the fine distribution of the TiO_{2-x} particles (inset figure shows the particle size distribution of TiO_{2-x}), (B) High magnification HRTEM images, (C) HRTEM lattice fringe image, (D) SAED pattern (scale bar 5 $1/\text{nm}$), (E) Dark-field HRTEM image of $\text{TiO}_{2-x}\text{@COF-Aq}$ (F) FESEM-EDS mapping images.

nanocomposite. The interplanar spacing of the nanoparticles was found to be approximately 0.35 nm, corresponding to the anatase (101) form of TiO_2 . The presence and uniform distribution of TiO_2 nanoparticles were also confirmed by SEM-EDS mapping results shown in Fig. 2F. The size of unsupported oxygen vacant TiO_{2-x} particle was found to be 69 ± 16 nm which is much larger compared to TiO_{2-x} on the COF-Aq support (Fig. S3, Supp. Info.). The formation and stabilization of relatively small-sized nanoparticles on the surface can be attributed to the higher surface area and abundant functional sites on the COF-Aq, providing adequate anchoring sites for nucleation and growth of nanoparticles [42]. From the ICP-MS analysis, the metal percentage was estimated to be 9.32 wt%, which further explains the facile nucleation and growth of nanoparticles resulting from strong hydrogen bonding between electronegative atoms (e.g., N, O) in the COF and TiO_2 .

The crystalline nature of COF-Aq and $\text{TiO}_{2-x}\text{@COF-Aq}$ was determined through PXRD pattern analysis, as shown in Fig. 3(A). As expected, the experimental PXRD pattern of COF-Aq exhibited a more intense prominent peak at 3.5° , indicating the presence of the (100) plane, along with two other lower intense diffraction peaks at 5.9° and 7.0° corresponding to the (110) and (210) crystal planes, respectively [43]. Additionally, a broad peak at around $2\theta = 25.8^\circ$ for COF-Aq indicated the Miller plane (001) reflection, resulting from the 2D π - π stacking arrangement between adjacent aromatic rings within the COF-Aq framework. The vertical distance between two close layers was approximately 3.45 Å, calculated from the d-spacing of the (001) plane. Rietveld refinement was carried out for refining the experimental PXRD pattern with unit cell parameters of $a = b = 29.8330$ Å, $c = 3.6214$ Å, $\alpha = \beta = 90^\circ$, and $\gamma = 120^\circ$ (residuals $R_{\text{wp}} = 12.8\%$ $R_{\text{exp}} = 5.8\%$; Fig. S4, Table S1: Supp. Info.). The refined pattern demonstrated good agreement with the experimental pattern. The PXRD pattern of

$\text{TiO}_{2-x}\text{@COF-Aq}$ showed the presence of all diffraction patterns observed for COF-Aq, supporting the experimental findings of the retained morphology of COF framework after nanoparticle synthesis. $\text{TiO}_{2-x}\text{@COF-Aq}$ exhibited five additional characteristic diffraction peaks around 26.2° , 38.4° , 48.7° , 54.1° , and 55.7° , corresponding to the indices of (101), (004), (200), (105), and (211) crystal planes, respectively. These peaks were consistent with the anatase phase crystal structure of TiO_2 (JCPDS No. 84-1286). The relatively low-intense peak of TiO_2 nanoparticles could be attributed to their low content or small size in the selected area.

To confirm the chemical structure of COF-Aq, we performed ^{13}C cross-polarization/magic-angle spinning (CP-MAS) solid-state nuclear magnetic resonance (NMR) spectroscopy and the results are shown in Fig. S5 (Supp. Info.). The resonance peak at ~ 180 and ~ 184 ppm corresponds to the keto group of anthraquinone and carbonyl group of keto-enol tautomer of COF-Aq, respectively. Likewise, the presence of peaks at ~ 145 and ~ 110 ppm was attributed to the enamine carbon ($=\text{C-NH-}$) and α -enamine carbon of COF-Aq, respectively. The aromatic carbons of the anthraquinone linkers resonate around ~ 130 ppm, confirming the successful formation of desired COF-Aq. These observations are in agreement with the previously reported anthraquinone based COFs [44]. FT-IR spectra shown in Fig. S6 (Supp. Info.) revealed the disappearance of the C=O stretch at 1655 cm^{-1} from TFG and the -NH band at 3236 cm^{-1} from diamine, confirming the reaction progress. The appearance of a strong absorption band at 1259 cm^{-1} , corresponding to the C-N stretch of the imine linkage, demonstrated the formation of COF-Aq [45]. Moreover, vibrational bands at 1595 cm^{-1} , 1545 cm^{-1} , and 1444 cm^{-1} were attributed to the aromatic (C=C) stretching of COF-Aq. No significant difference was observed in the FTIR spectra of $\text{TiO}_{2-x}\text{@COF-Aq}$, suggesting the unaltered chemical nature of COF-Aq

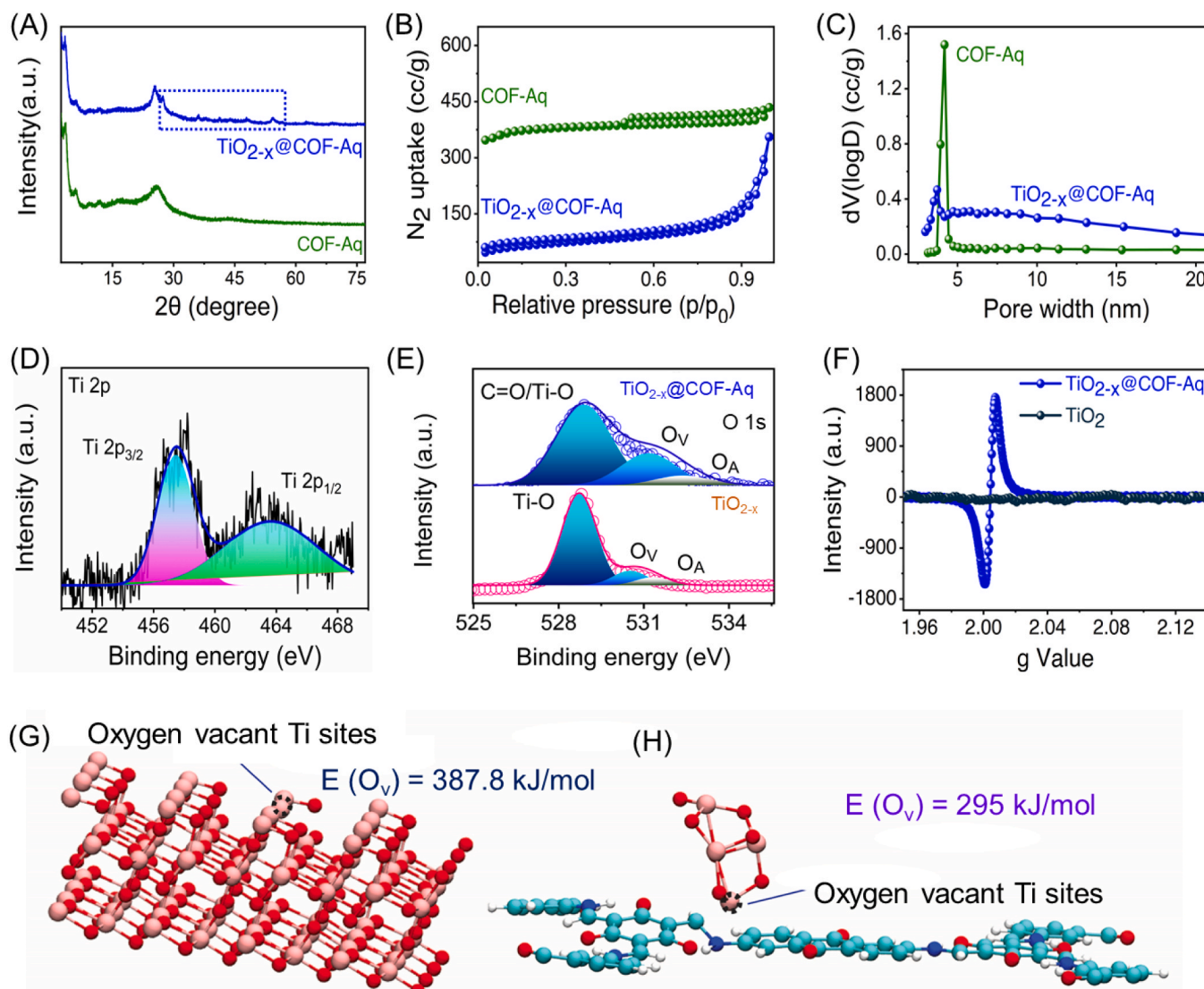


Fig. 3. (A) PXRD spectra of COF-Aq and $\text{TiO}_{2-x}\text{@COF-Aq}$, (B) N_2 adsorption/desorption isotherm, (C) pore size distribution of COF-Aq and $\text{TiO}_{2-x}\text{@COF-Aq}$. High-resolution X-ray photoelectron deconvoluted spectra of: (D) 2p Ti of $\text{TiO}_{2-x}\text{@COF-Aq}$ and (E) deconvoluted high resolution O 1s spectra of TiO_{2-x} and $\text{TiO}_{2-x}\text{@COF-Aq}$. (F) ESR spectra of $\text{TiO}_{2-x}\text{@COF-Aq}$ and TiO_2 . (G) DFT calculations for oxygen vacancy formation energy on the pure TiO_{2-x} surface, and (H) $\text{TiO}_{2-x}\text{@COF-Aq}$. (The schematics represent the oxygen vacant sites at anatase TiO_{2-x} and TiO_{2-x} nanocluster mounted on the COF-Aq).

after modification with nanoparticle. The N_2 adsorption/desorption isotherms of synthesized compounds are demonstrated in Fig. 3(B and C). COF-Aq exhibited type IV adsorption isotherms with a tiny hysteresis loop. The continuous increment of pressure within the region 0.4–1 (P/P_0) with a hysteresis loop indicated the presence of permanent mesopores in the COF-Aq . The total pore volume of COF-Aq and $\text{TiO}_{2-x}\text{@COF-Aq}$ was estimated to be $0.62 \text{ cm}^3/\text{g}$ and $0.51 \text{ cm}^3/\text{g}$, respectively, while the BET surface area was found to be $1180 \pm 150 \text{ m}^2/\text{g}$ and $244.287 \pm 30 \text{ m}^2/\text{g}$ (average of 3 samples), respectively. The pore size distribution, estimated based on the Barrett-Joyner-Halenda model, was found to be 4.176 nm and 3.708 nm for COF-Aq and $\text{TiO}_{2-x}\text{@COF-Aq}$, respectively. However, the lower surface area of $\text{TiO}_{2-x}\text{@COF-Aq}$ with minimal change in pore diameter signified the uniform distribution of TiO_2 throughout the COF-Aq matrix. It is worth mentioning that the surface area of the nanocomposite $\text{TiO}_{2-x}\text{@COF-Aq}$ is significantly higher than the bulk TiO_{2-x} (Fig. S8, Supp. Info.). The porous characteristics of $\text{TiO}_{2-x}\text{@COF-Aq}$ provide a suitable system for catalytic reactions, allowing rapid mass transport during the reaction. Fig. S9 (Supp. Info.) shows the thermal stability of the synthesized COF samples in an N_2 environment. A significant weight

loss between 105 and 230°C corresponded to the loss of adsorbed water and residual solvent molecules in the COF matrix. However, COF-Aq retained 85% of its initial mass at 520°C . The improved thermal stability of COF-Aq after modification with TiO_2 can be attributed to the strong interaction between COF-Aq and TiO_2 , which prevents the decomposition of the COF framework.

To investigate the surface composition, valance state, metal-support interaction, and oxygen defects in $\text{TiO}_{2-x}\text{@COF-Aq}$, X-ray photoelectron spectroscopy (XPS) was performed. The XPS survey spectra, depicted in Fig. S10 (Supp. Info.), provided evidence of different energy levels of C, N, O, and Ti. The deconvoluted spectra of C 1s at 282.8 eV correspond to the imine ($-\text{C}=\text{N}-\text{C}$) bonds of COF skeletal and confirm the synthesis of imine-based COF [46]. In the N 1s spectra, the peak at 399.28 eV refers to the Ti-N linkage and also confirm that the imine sites of COF-Aq serve as binding sites for anchoring TiO_{2-x} nanoparticles (Fig. S11, Supp. Info.) [47]. Broadening in the N 1s spectra in the case of $\text{TiO}_{2-x}\text{@COF-Aq}$ compared to neat COF-Aq indicates the formation of a new Ti-N bonds. Compared to COF-Aq , the binding energy of N 1s peak in $\text{TiO}_{2-x}\text{@COF-Aq}$ demonstrates a positive shift (Fig. S12, Supp. Info.). This indicates a charge-transfer between the COF-Aq framework and

TiO₂ nanoparticle as a result of SMSI effect [48]. In the Ti 2p deconvoluted spectra (Fig. 3D), two broad XPS bands at 457.9 and 464.9 eV correspond to Ti 2p_{3/2} and Ti 2p_{1/2}, respectively, confirming the presence of Ti⁴⁺ sites. Additionally, a prominent peak at a binding energy of 457.42 eV signifies the presence of Ti³⁺, resulting from the formation of oxygen-deficient sites (Fig. S13A, Supp. Info.) [49]. The concentration of Ti³⁺ was determined through peak area of Ti 2p spectra, and was found to be 39% in the TiO_{2-x}@COF-Aq. The existence of a high concentration of Ti³⁺ indicates the presence of abundant oxygen vacant sites [50]. In contrast, the presence of both Ti³⁺ and Ti⁴⁺ signifies that COF-Aq framework strongly interacted with the TiO_{2-x} nanoparticles [51]. The SMSI between the COF-Aq and TiO₂ nanoparticles not only facilitates the electron transport phenomenon but also enhances the stability of catalyst during long-term operation. The availability of higher oxygen vacancy concentration can effectively perturb the overall electronic environment by enhancing the composite's electrical conductivity and making Ti center electron rich. Moreover, the downshifting of binding energy of Ti (IV) 2p_{3/2} spectra in TiO_{2-x}@COF-Aq compared to neat TiO₂ is attributable to the availability of reduced Ti sites. The presence of oxygen defect sites was further confirmed by the fitted O 1s spectra at ~531 eV, shown in Fig. S13B (Supp. Info.), corresponding to the oxygen vacant sites of TiO_{2-x}. The oxygen vacancy (O_v) percentage was calculated from O 1s spectra peak area and found to be ~26% for TiO_{2-x}@COF-Aq, which is remarkably higher than the oxygen vacancy present in the bulk oxygen vacant TiO_{2-x} (12.52%) (Fig. 3E) [52,53]. Electron paramagnetic resonance (EPR) spectroscopy was performed to gain insight information about the oxygen vacancy formation, primarily supported by the XPS analysis. As shown in Fig. 3F, a prominent EPR signal at g value of 2.004 was observed for TiO_{2-x}@COF-Aq, confirming the presence of Ti³⁺ sites, and the intensity of the EPR signal is comparatively higher than the bulk oxygen vacant TiO_{2-x}. A nearly 1.5 times higher intense EPR signal for TiO_{2-x}@COF-Aq as compared to the bulk oxygen vacant TiO_{2-x}, signifies a higher concentration of oxygen vacant sites in the earlier (Fig. S14, Supp. Info.) [22]. An upsurge in oxygen vacancy concentrations in TiO_{2-x}@COF-Aq can be accredited to the strong metal-support interaction between COF-Aq and TiO_{2-x} at the interface, nanosized TiO_{2-x} and abundant Ti³⁺ sites, resulting from the facile electron transfer from COF-Aq support to TiO₂. Additionally, Raman analysis was conducted to assess the formation of oxygen vacancies in both TiO_{2-x} and TiO_{2-x}@COF-Aq. The corresponding results are illustrated in Fig. S15 (Supp. Info.). The Raman spectra showed a noticeable red shift and increased spectral width in the E_g peak of TiO_{2-x}@COF-Aq compared to pristine TiO_{2-x}, likely attributed to phonon confinement effects induced by localized defects [22,54]. These findings further confirm the enhancement in oxygen vacancy concentration in TiO_{2-x}@COF-Aq compared to TiO_{2-x}, consistent with the results obtained from XPS and EPR analyses.

The optoelectronic properties of the TiO_{2-x}@COF-Aq were addressed by diffuse reflectance UV-visible spectroscopy, and results are shown in Fig. S16 (Supp. Info.). Such a broad absorption range in the visible region and red shifting in wavelength indicates the presence of sufficient oxygen-vacant sites and strong metal-support interaction. Subsequently, Tauc plot analysis revealed that TiO_{2-x}@COF-Aq exhibited a lower band gap (2.803 eV) in comparison with TiO_{2-x} (3.01 eV), as shown in Fig. S16B. The lowered band gap facilitates the hopping electron transfer from the catalyst to the reactant intermediates. Following which, DFT calculations are performed to estimate the energetics of oxygen vacancy formation on the surfaces of pure TiO₂ and TiO₂ supported on COF-Aq. The results are represented in Fig. 3 (G, H), wherein a significantly lower oxygen vacancy formation energy is estimated for TiO_{2-x} on COF-Aq (295 kJ/mol) as compared to pure TiO_{2-x} (388 kJ/mol) surface. A similar value of oxygen vacancy formation energy on pure TiO₂ surface is reported by Robertson and co-workers [55]. Oxygen vacancies are likely to form in higher concentration on COF-Aq supported TiO₂ due to reduced energetics, as compared to pure TiO₂ which is consistent with the XPS, EPR and Raman

analysis. On account of the higher concentration of oxygen vacant sites, surface area, copious active sites, and lowered band gap structure, the as-synthesized catalyst can be a suitable alternative for achieving high-performance ENRR activity.

4. Electrochemical nitrogen fixation

The ENRR performance was analyzed under ambient temperature and pressure conditions in 0.1 M HCl using a two-compartment cell (H-Type) separated by a proton exchange membrane (Fig. S17, Supp. Info.). Unless otherwise specified, all the ENRR experiments were performed using a three-electrode system consisting of platinum as the counter electrode, Ag/AgCl as the reference electrode, and all the potentials were converted to RHE. The setup was connected to a high-purity nitrogen cylinder, and the N₂ flow was regulated using a gas flow controller. To avoid the loss of NH₃ as a result of N₂ flow, an absorber was connected at the end of the cell. The ammonia concentration was quantified by colorimetric method (Indophenol method) using standard NH₄Cl solutions and the possible hydrazine product was detected by the Watt and Chrisp method. Before performing electrocatalytic NRR, linear sweep voltammetry (LSV) was performed under Ar and N₂ saturated 0.1 M HCl electrolyte. LSV polarization curves showed increased current density in N₂ saturated solution as compared to Ar saturated electrolytes, suggesting favorable conditions for the ENRR process (Fig. S18, Supp. Info.). In Ar-saturated conditions, the increment in cathodic currents with applied negative potential can be primarily attributed to the hydrogen evolution reaction [56,57]. No observable ammonia was detected in the case of carbon black, as shown in Fig. S19 (Supp. Info.), whereas the LSV polarization curve of, TiO_{2-x}@COF-Aq (Fig. 4A) exhibits much higher current density in comparison with COF-Aq and TiO_{2-x}. The origin of such higher current density in the case of TiO_{2-x}@COF-Aq is attributed to its higher no. of active center, higher surface area, and strong metal-support interaction. Chronoamperometry was performed at different potentials ranging from -0.1 to -0.75 V vs RHE to examine the ENRR efficiency of TiO_{2-x}@COF-Aq, results are shown in Fig. 4B. During this process, N₂ molecules are adsorbed onto the electrocatalyst's surface, combining with protons and electrons to form NH₃ molecules followed by desorption from the electrocatalyst's surface. After 1 h of electrolysis under N₂ purged condition, an aliquot of electrolyte was taken out and stained with indophenol indicator prior to collection of the UV-vis spectra presented in Fig. 4C. A distinct absorbance at ~665 nm validates the ENRR process, and a relatively higher absorbance at a potential of -0.5 V vs RHE, was observed due to higher NH₃ concentration at this potential. Subsequently, based on standard calibration of UV-vis spectra (Fig. S20, Supp. Info.), ammonia yield and Faradaic efficiency (FE) were calculated (Fig. 4D). Detailed observations and analysis of electrochemical studies have revealed that the NH₃ yield and FE were increased with applied potential, and the maximum NH₃ yield (30 µg/h mg) and FE (~16%) were detected at -0.5 V vs RHE, which are almost 3.22 and 2.5 times higher than bulk oxygen vacant TiO_{2-x} (9.1 µg/h mg and 6.2%, Fig. S21, Supp. Info.) respectively. Beyond this potential (-0.5 V vs RHE), a notable drop in NH₃ yield along with FE was observed (Fig. S22, Supp. Info.), possibly due to the competitive HER process. Unless otherwise mentioned, all the electrochemical NRR data shown here are presented after three consecutive repetitions to avoid the experimental error. Additionally, the possible by-product hydrazine hydrate during the NRR process was detected using Watt and crisp method. The UV-vis spectra of electrolytes did not show any absorbance maxima at ~460 nm, assuring the absence of undesired hydrazine hydrate product (Fig. S23, Supp. Info.). This also validates the selectivity of the designed catalyst (TiO_{2-x}@COF-Aq) towards electrochemical nitrogen reduction reaction for the direct production of ammonia.

To confirm that the NH₃ production originated from the ENRR process using our designed catalyst, we conducted a variety of control experiments, including (1) no electrocatalysts placed in the electrolyte, (2)

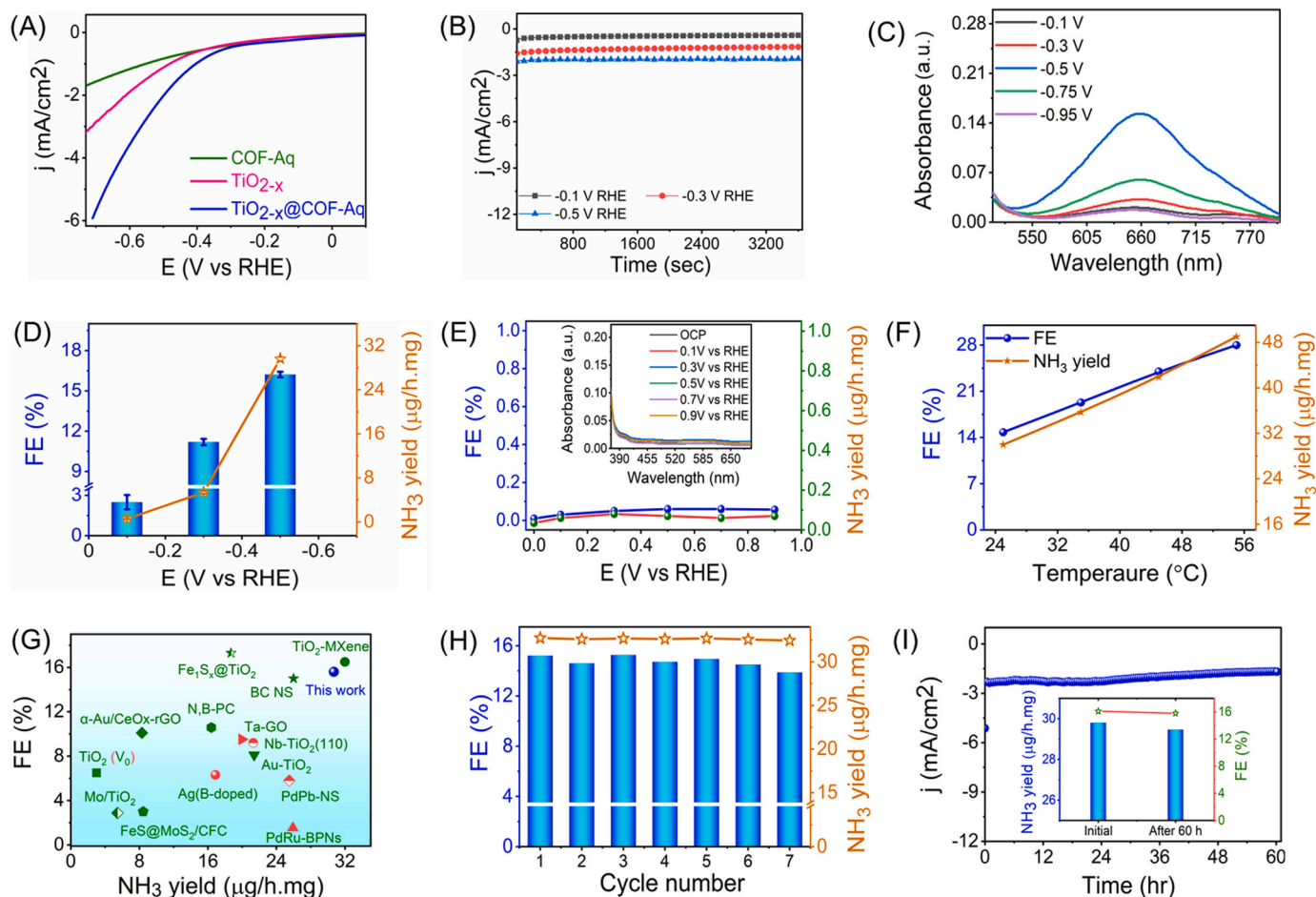


Fig. 4. ENRR performance for COF-Aq, TiO_{2-x} , and $\text{TiO}_{2-x}@\text{COF-Aq}$ in N_2 saturated electrolytes (0.1 M HCl , $\text{pH } 1$). (A) LSV curves of COF-Aq, TiO_{2-x} , and $\text{TiO}_{2-x}@\text{COF-Aq}$ measured under N_2 atmosphere, (B) chronoamperometry data at various potential for 1 h, (C) corresponding UV–visible spectra of electrolytes recorded after stained with indophenol indicator. NH_3 yield and Faradaic efficiency (FE) of $\text{TiO}_{2-x}@\text{COF-Aq}$ (D) at a different potential, (E) under Ar atmosphere at different potential (corresponding UV–vis spectra of electrolytes at different potential shows in inset figure), (F) different temperatures at -0.55 V vs. RHE, (G) comparison of ENRR activity with the state-of-the-art NRR electrocatalyst in 0.1 M HCl at room temperature, (H) cycling test of $\text{TiO}_{2-x}@\text{COF-Aq}$ at -0.5 V vs. RHE, (I) long-term chronoamperometry curves at -0.5 V vs. RHE (inset figure shows the initial and post- NH_3 yield and FE).

electrolysis carried out under N_2 -saturated conditions (at OCP) for 2 hr, and (3) electrolysis carried out under Ar-saturated conditions (at -0.5 V Vs RHE). As shown in Figs. S26–S28 (Supp. Info.), no ammonia generation was detected in any of the control experiments. The primary evidence of catalyst selectivity was obtained when traces of ammonia were not detected under electrolysis of Ar-saturated electrolyte at different potentials (Fig. 4E). Furthermore, no traces of hydrazine hydrate were detected after the electrolysis at different potentials, confirming the extraordinary selectivity of the catalyst towards ammonia (Fig. S29, Supp. Info.). To ensure that the electrolyte medium was free of nitrate contaminants before electrolysis, considering the potential conversion of nitrate contaminants (NO_2^- and NO_3^-) to ammonia during the ENRR, we conducted tests as shown in Fig. S30 (Supp. Info.). Moreover, the ammonia yield and FE of $\text{TiO}_{2-x}@\text{COF-Aq}$ were determined through a cyclic ENRR test by alternating between N_2 -saturated and Ar-saturated electrolytes (Fig. S31, Supp. Info.). The results validated that the ammonia yield was only detected in N_2 conditions, with no ammonia detected during the switch to Ar-saturated electrolytes. These observations confirm that ammonia production is solely occurring from supplied N_2 as the N source in the ENRR process and is facilitated by $\text{TiO}_{2-x}@\text{COF-Aq}$ as the electrocatalyst. The rate of NH_3 yield and FE was increased nearly 1.6 and 1.8 times when the temperature of the electrolytes was increased from 25° to 55°C . Following the trends of the Arrhenius equation, the enhanced catalytic activity can be well

attributed to the increased mass transfer of reactant at elevated temperature (Fig. 4F). By solving the Arrhenius equation, the activation energy of the electrocatalyst was quantified to be 12.88 kJ/mol (Fig. S32, Supp. Info.). Such low activation energy requirement of the catalyst manifests its potential to be used as an alternative approach to the traditional energy-intensive Haber–Bosch process.

To have a fair comparison of $\text{TiO}_{2-x}@\text{COF-Aq}$ with previously reported ENRR electrocatalyst in the 0.1 M HCl electrolyte, NH_3 yield, and FE index were taken as a basis for comparison (Fig. 4G). A detailed comparison is shown in Table S2, Supp. Info. where the $\text{TiO}_{2-x}@\text{COF-Aq}$ stands out among the reported catalysts with significantly high ammonia yield and FE. In this regard, the turn-over frequency of the catalyst was calculated and compared with the bulk oxygen vacant TiO_{2-x} at maximum NH_3 yield; results illustrated that the $\text{TiO}_{2-x}@\text{COF-Aq}$ exhibits almost 13 times higher TOF values compared with the TiO_{2-x} (0.06 h^{-1}) (Fig. S33, Supp. Info.). Moreover, the ENRR activity of $\text{TiO}_{2-x}@\text{COF-Aq}$ outpaces the traditional noble metal-based electrocatalyst for NRR reaction [58–60]. The high tenacity of $\text{TiO}_{2-x}@\text{COF-Aq}$ was verified by performing multiple ENRR cycles, and the obtained NH_3 yield and FE in the different cycles are presented in Fig. 4H. No significant decay in NH_3 yield as well as FE was observed during seven consecutive cycles. The potential candidacy of $\text{TiO}_{2-x}@\text{COF-Aq}$ was further verified by a long-term chronoamperometry study, showing no noticeable drop in the current density after a continuous operation for

60 h with a maintained NH_3 yield with FE (Fig. 4I). To verify the stability of electrocatalyst after long-term ENRR study, we have performed several post-catalysis studies, and the results are shown in Fig. S34 (Supp. Info.). As shown in Fig. S34A and S34D (Supp. Info.), there were no noticeable changes in PXRD and EPR pattern, suggesting that the structural features remain intact after the ENRR cycle. Furthermore, XPS analysis of TiO_{2-x} @COF-Aq after ENRR measurements indicated that the valence state of Ti remained unchanged (Fig. S34B, Supp. Info.). The TEM images (Fig. S34C) revealed that the TiO_{2-x} @COF-Aq catalyst largely maintained its structure, with no evidence of nanoparticle agglomeration after prolonged electrolysis. Additionally, no significant traces of metal leaching were observed during extended operation (Fig. S34E, Table S3, Supp. Info.), ruling out concerns of catalyst degradation/leaching or environmental interference in ammonia production. Elemental mapping images show that all the elements are still homogeneously distributed over the entire TiO_{2-x} @COF-Aq sample after long-term ENRR activity (Fig. S34F, Supp. Info.). The superior stability can be attributed to the strong interaction between the

nanoparticle and COF-Aq support, preventing migration or aggregation for small-sized and uniformly distributed TiO_2 nanoparticles.

4.1. Origin of enhanced stability: effect of nanosized oxygen vacant TiO_{2-x} on COF-Aq support

To uncover the enhanced electrochemical NRR activity and electronic environment of TiO_{2-x} @COF-Aq, several experimental and theoretical analyses were performed. Electrochemical impedance spectroscopy revealed a lower charge transfer resistance for TiO_{2-x} @COF-Aq compared to bulk oxygen vacant TiO_{2-x} (Fig. 5A), suggesting that the developed nanocomposite catalyst requires a much lower activation barrier to facilitate the overall ENRR process. The electrochemically active surface area of TiO_{2-x} and TiO_{2-x} @COF-Aq were also examined in the non-faradaic region of the CV cycle, and the double-layer capacitance (C_{dl}) of catalysts was calculated. As shown in Fig. 5B, the C_{dl} value of TiO_{2-x} @COF-Aq (3.06 mF/cm^2) is much higher than that of TiO_{2-x} (0.89 mF/cm^2), implying the presence of higher no. of electroactive sites

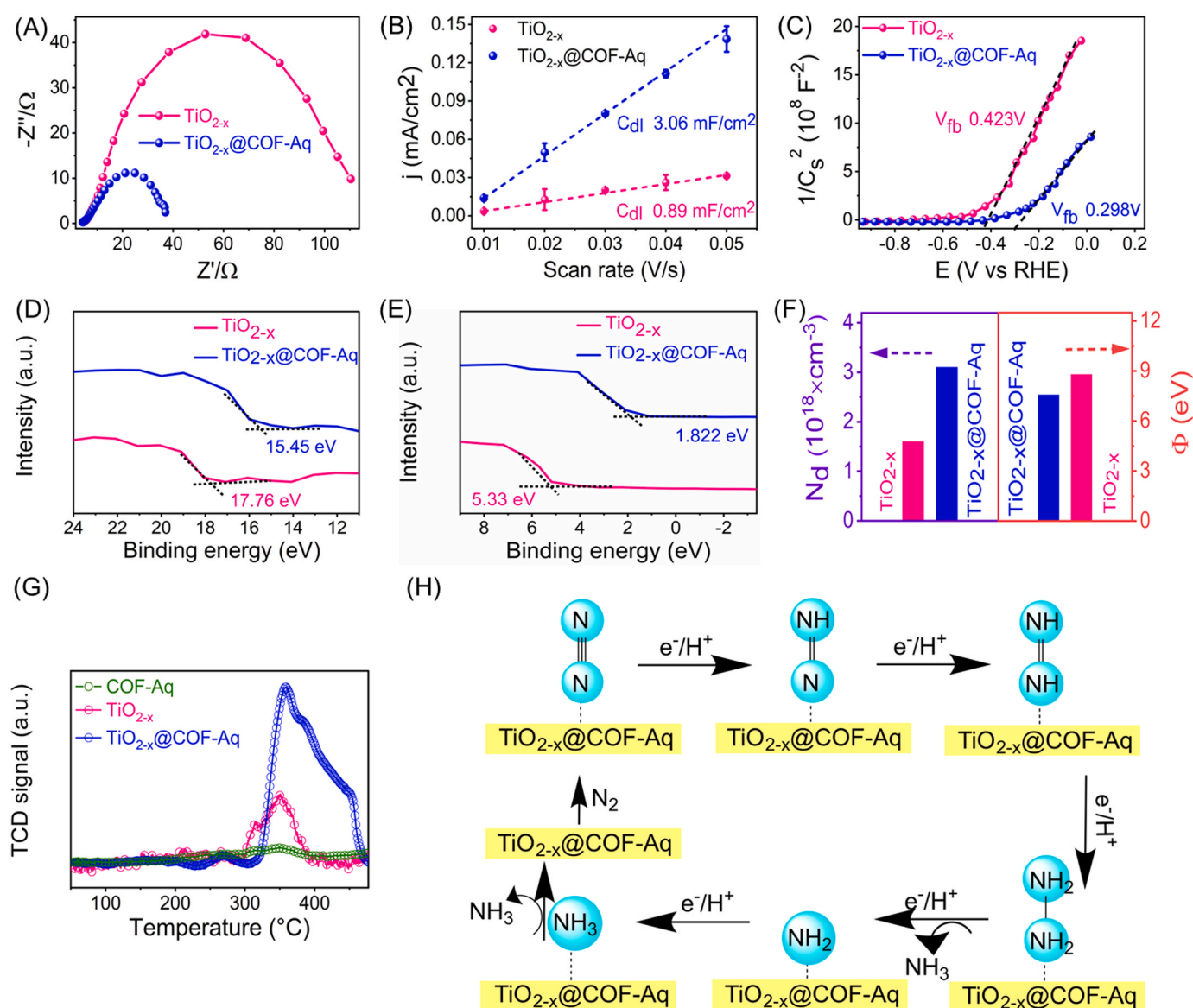


Fig. 5. (A) Nyquist plots, (B) CV at different scan rates in the non-faradaic region of TiO_2 and TiO_{2-x} @COF-Aq, (C) Mott-Schottky experiment with TiO_{2-x} and TiO_{2-x} @COF-Aq in 0.1 M HCl. UPS spectra in the (D) secondary electron cutoff energy (E_{cutoff}) regions and (E) onset energy (E_{onset}) regions of TiO_{2-x} and TiO_{2-x} @COF-Aq, (F) calculated donor density (N_d) and work function calculated from the Mott-Schottky and UPS analysis, respectively, (G) N_2 TPD profiles of TiO_{2-x} and TiO_{2-x} @COF-Aq, (H) schematic representation of the electrochemical NRR process on TiO_{2-x} @COF-Aq.

in nanosized oxygen vacant $\text{TiO}_{2-x}\text{@COF-Aq}$ in comparison to bulk TiO_{2-x} . To probe the role of oxygen vacancies in the ENRR process, TiO_2 nanoparticle without oxygen vacancy was synthesized on the COF-Aq using similar method without calcination [32]. The absence of oxygen vacancy on $\text{TiO}_2\text{@COF-Aq}$ was confirmed through the EPR analysis (Fig. S36A, Supp. Info.). As shown in Fig. S36D, $\text{TiO}_2\text{@COF-Aq}$ exhibited significantly lower N_2 adsorption capacity despite its similar structural and morphological features compared to $\text{TiO}_{2-x}\text{@COF-Aq}$. Moreover, the NH_3 yield of $\text{TiO}_2\text{@COF-Aq}$ was found to be $\sim 5 \mu\text{g/h.mg}$, which is substantially lower than that of oxygen vacant $\text{TiO}_{2-x}\text{@COF-Aq}$ (Fig. S36E, Supp. Info.). This difference can be attributed to the limited availability of active sites in $\text{TiO}_2\text{@COF-Aq}$, which hinders its ability to facilitate the N_2 adsorption and the ENRR processes. Overall, the vacancy rich $\text{TiO}_{2-x}\text{@COF-Aq}$ catalyst exhibits remarkable ENRR activity, surpassing the performance of previously reported state-of-the-art NRR electrocatalysts. Based on these observations, we inferred that the large number of oxygen vacant sites on the $\text{TiO}_{2-x}\text{@COF-Aq}$ serves as the active sites for ENRR reaction, which was further supported by previously reported studies [61,62]. An assumption on the role of COF-Aq not only as a support but for synergistic enhancement in the catalytic activity of oxygen vacant TiO_{2-x} has to be verified through experimental evidence. The best way to explain the synergism is by quantifying the electronic perturbation occurring because of the stabilization of nanoparticles. COF-Aq supports not only provides sufficient nucleating sites for nanoparticle growth but also affects the overall composite's electronic band structure due to its planar two-dimensional structure with inherent conductivity. Indeed, electron band modification of composites alters the surface work function, which induces a facile charge-transfer phenomenon between the catalyst's surface and intermediates to enhance the electrocatalytic activity. Several experimental analyses have been performed, including Mott-Schottky analysis, UV-vis spectroscopy, and ultraviolet photoelectron spectroscopy (UPS), to scrutinize the role of the oxygen vacant TiO_{2-x} on COF-Aq interface. The positive slope obtained from the Mott-Schottky analysis indicates the n-type semiconductor nature of oxygen vacant bulk TiO_{2-x} . Interestingly, the flat-band potential was decreased to 0.298 V for $\text{TiO}_{2-x}\text{@COF-Aq}$ which is lower compared to the TiO_{2-x} (0.423 V), primarily indicating a lower work function of the final nanocomposite catalyst (depicted in Fig. 5C). From the Mott-Schottky analysis, the donor density was estimated to be 1.6×10^{18} and $3.1 \times 10^{18} \text{ cm}^{-3}$ for TiO_{2-x} and $\text{TiO}_{2-x}\text{@COF-Aq}$, respectively (Fig. 5F). The higher donor density can be attributed to the abundant oxygen vacant concentration, which eases the electron transfer phenomenon, amplifying the overall ENRR activity [63]. UPS analysis was conducted to find the $E_{\text{cut-off}}$ energy and E_{onset} energy. Subsequently, the work function (Φ) was estimated using equation $\Phi = h\nu - (E_{\text{cut-off}} - E_{\text{onset}})$, where $h\nu$ (21.22 eV) is the excitation light's photon energy. As depicted in Fig. 5F, the work function of $\text{TiO}_{2-x}\text{@COF-Aq}$ (7.56 eV) is smaller compared to the bulk oxygen vacant TiO_{2-x} (8.79 eV). The lower work functions of the final nanocomposite catalyst can be attributable to the strong metal-support interaction at the interface whereas lower flat band potential and higher donor density, result in enhanced electron transfer process at the Fermi level. Generally, a lower work function of a catalyst provides a low-energy barrier for electron transfer between the catalyst to adsorbed N_2 molecules and reaction intermediates, thereby boosting the ENRR activity [64,65]. As the primary step for the ENRR process is the adsorption of dinitrogen molecules on the catalyst's active sites, the $\text{TiO}_{2-x}\text{@COF-Aq}$ exhibits a stronger and more prominent signal than the bulk oxygen vacant TiO_{2-x} . This suggests that the nanosized well-distributed TiO_{2-x} grown on COF-Aq provides sufficient exposed sites to adsorb N_2 molecules (Fig. 5G) [66]. We further demonstrated the superior N_2 adsorption capacity of $\text{TiO}_{2-x}\text{@COF-Aq}$ in 0.1 M HCl electrolyte through an in-situ operando FTIR analysis, as shown in Fig. S37 (Supp. Info.). In a nitrogen saturated electrolyte solution, the catalysts were operated at -0.5 V potential and formation of N-N intermediate via adsorption of N_2 molecule was confirmed with the appearance of

absorbance peak at $\sim 1110 \text{ cm}^{-1}$ (corresponding to the N-N stretching frequency) on both $\text{TiO}_{2-x}\text{@COF-Aq}$ as well as TiO_{2-x} catalyst surfaces. The higher intensity of the 1110 cm^{-1} absorbance peak for $\text{TiO}_{2-x}\text{@COF-Aq}$ compared to pristine TiO_{2-x} further supports the claim of an enhanced N_2 adsorption tendency on the modified catalyst surface due to its increased oxygen vacancy concentration [67,68].

Summarizing the above experimental observations, it can be postulated that the superior ENRR activity of $\text{TiO}_{2-x}\text{@COF-Aq}$ can be attributed to its numerous oxygen vacant sites originating from the small-sized TiO_{2-x} nanoparticle supported over the COF-Aq substrate. The inherent conductive nature of COF-Aq further facilitates the charge-transfer phenomenon during the ENRR process. Moreover, the strong interaction between the TiO_{2-x} nanoparticle and COF-Aq support prevents metal leaching during the long-term ENRR activity.

4.2. Mechanistic insights

In order to gain mechanistic insights into the electrochemical N_2 reduction, DFT simulations were performed. It is generally accepted that the first step in activating the NRR is the adsorption of N_2 molecules on the catalyst surface. For this purpose, periodic slabs of TiO_2 (101) with N_2 adsorbed at the oxygen vacant site (O_v) are compared with the H atom adsorption Fig. 6 (A). We initially screened the preferred N_2 adsorption site by calculating the N_2 adsorption energy at various sites on TiO_{2-x} using DFT calculations. Fig. S39 (section S13.2, Supp. Info.) shows that oxygen vacant sites ($\text{Ti}_{\text{O.vac}}$) bind N_2 much more favorably than the bridging site between the two Ti atoms (Ti_b) and the top side of the oxygen atom (O_t). In addition, we explored the role of oxygen vacancies on N_2 adsorption by calculating N_2 adsorption energy on oxygen vacant $\text{TiO}_{2-x}\text{@COF-Aq}$ and without oxygen vacant $\text{TiO}_2\text{@COF-Aq}$ (Fig. S40, section S13.3, Supp. Info.). The study revealed that the surface without oxygen vacancies requires significantly more energy to adsorb N_2 ($E_{\text{ads}}(\text{N}_2) = 78 \text{ kJ/mol}$) compared to oxygen vacant TiO_{2-x} ($E_{\text{ads}}(\text{N}_2) = 108 \text{ kJ/mol}$). To study the effect of the TiO_{2-x} nanocluster on the adsorption of N_2 & H, the nanocluster of TiO_{2-x} is mounted on the $\text{TiO}_{2-x}\text{@COF-Aq}$ Fig. 6 (B) & (C). In addition, two alternative orientations for N_2 adsorption on TiO_{2-x} referred to as end-on and side-on are studied, as they were utilized for the subsequent N_2 reduction in previous studies [20]. In the end-on structure, the $\text{N}\equiv\text{N}$ bond is nearly perpendicular to the surface and is considered to be a preferable mode of adsorption with a 11 kJ/mol higher binding energy than the side-on structure. N_2 is calculated to adsorb stronger on the $\text{TiO}_{2-x}\text{@COF-Aq}$ structure with an adsorption energy ($E_{\text{ads}}(\text{N}_2)$) of -108 kJ/mol as compared to the oxygen vacant site on pristine TiO_{2-x} ($E_{\text{ads}}(\text{N}_2) = -81 \text{ kJ/mol}$) as shown in Fig. 6 (D). Further, we have noticed a minimal change in N_2 adsorption energy upon increasing the cluster size from $(\text{TiO}_2)_4$ ($E_{\text{ads}}(\text{N}_2) = 108 \text{ kJ/mol}$) to $(\text{TiO}_2)_{12}$ ($E_{\text{ads}}(\text{N}_2) = 96 \text{ kJ/mol}$) (Fig. S41, Section S13.4, Supp. Info.). This stronger binding of nitrogen on the $\text{TiO}_{2-x}\text{@COF-Aq}$ is evident in the shorter bond length of *N-Ti (2.4 \AA) than 2.8 \AA for N_2 adsorption at the O_v site (Fig. 6 (B) & (C)). This stronger interaction of nitrogen with the COF-modified TiO_2 surface is likely to result in greater catalytic activity.

Since HER is a dominant side reaction for the NRR, free energy of adsorption of atomic hydrogen on the catalyst was calculated, and the results are shown in Fig. 6D. The adsorption energy $E_{\text{ads}}(\text{H})$ was estimated to be -67 and -48 kJ/mol for $\text{TiO}_{2-x}\text{@COF-Aq}$ and TiO_{2-x} , respectively. Hydrogen is observed to bind relatively less stronger than nitrogen on both the TiO_{2-x} and $\text{TiO}_{2-x}\text{@COF-Aq}$ oxygen vacant sites as shown in Fig. 6 (D). The unusually strong N_2 adsorption on these structures distinguishes them as catalysts for achieving higher NRR selectivity vis-à-vis to the HER. The binding interaction of N_2 with the transition metal oxide is evident in charge analysis wherein the more negative charge on the adsorbed N_2 shows higher back donation of electrons from the metal to adsorbed nitrogen molecule. Restrained electrostatic potential (RESP) analysis of the charges on adsorbed N_2 and H on the TiO_{2-x} and $\text{TiO}_{2-x}\text{@COF-Aq}$ structure sites is shown in Fig. 6

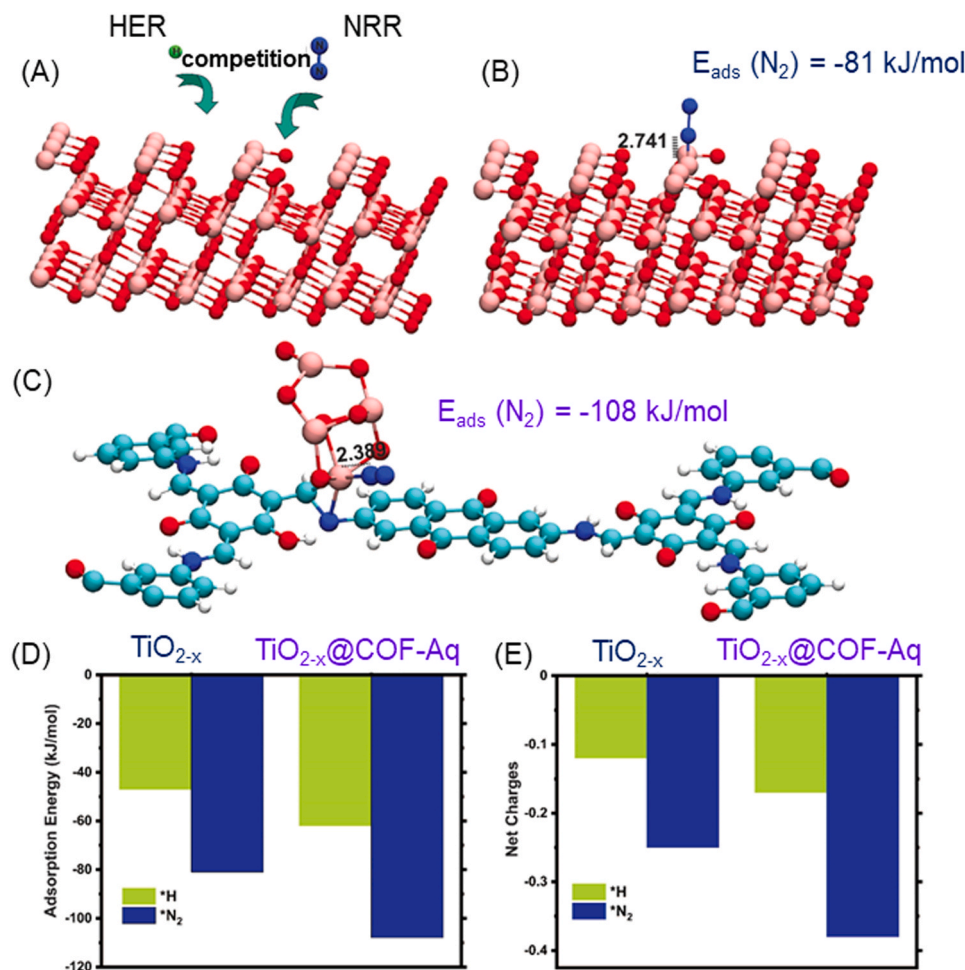


Fig. 6. (A) Competing adsorption of adsorption of N_2 and H for the NRR and HER (B) N_2 adsorbed on the oxygen vacant (O_v) TiO_{2-x} (101) sites and on (C) TiO_{2-x} cluster mounted on the covalent organic framework (TiO_{2-x} @COF-Aq), (D) Adsorption energies of H and N_2 molecule on TiO_{2-x} and TiO_{2-x} @COF-Aq, (E) shows the RESP charge analysis of N_2 and H after adsorption, where red, blue, cyan, white, and orange colors represent the oxygen, nitrogen, carbon, hydrogen, and titanium. Bond distances are shown in Å.

(E). The N_2 adsorbed at the TiO_{2-x} @COF-Aq has a greater negative charge than TiO_{2-x} , which is consistent with the adsorption trend at both systems. The net charge on the adsorbed N_2 could form a descriptor for nitrogen adsorption and overall NRR activity of the catalyst surface. Based on the experiments and theoretical observations, a schematic representation of a plausible mechanism for the ENRR process on the TiO_{2-x} @COF-Aq has been given in Fig. 5H. Initially, the N_2 molecule was preferably adsorbed on the vacant site of TiO_{2-x} , followed by electron transfer and consecutive protonation steps to form ammonia. From the DFT analysis, it has been confirmed that the N_2 is preferably adsorbed on the oxygen vacant sites of the TiO_{2-x} sites and prevents the H -adsorption, thereby facilitating the overall ENRR activity of the catalyst. The strong electronic interaction can effectively stabilize the adsorbates and reduce the thermodynamic energy barriers to enhance the NRR activity of TiO_{2-x} @COF-Aq. In addition to that, oxygen vacant sites on the TiO_{2-x} @COF-Aq provide an adequate active site to adsorb the N_2 molecule selectively, followed by the PCET without any hindrance. Corroborating experiments and DFT studies availability of abundant oxygen vacant sites on the nanocomposite catalyst (TiO_{2-x} @COF-Aq) for facilitating the N_2 adsorption over H_2 to promote the ENRR activity.

5. Conclusions

Our findings highlight the importance of designing nanosized oxygen

vacant TiO_{2-x} on a conductive COF-Aq, which promotes the ENRR activity and restricts the HER. In summary, we present a facile fabrication strategy to anchor nanosized oxygen vacant TiO_{2-x} on a COF support using a hydrothermal-calcination approach for electrocatalytic NRR. The formation of oxygen vacant TiO_{2-x} is thoroughly characterized using several techniques, and it was found that the oxygen vacancy concentration of nanocomposite TiO_{2-x} @COF-Aq is higher than that of bulk TiO_{2-x} . Moreover, DFT analysis suggests that the TiO_{2-x} @COF-Aq requires lower oxygen vacancy formation energy than pristine TiO_{2-x} , thereby increasing the oxygen vacancy concentration which is line with the EPR and XPS analysis. The defect-rich TiO_{2-x} @COF-Aq electrocatalyst exhibits a high NH_3 yield rate of $30 \mu\text{g mg}^{-1}\text{h}^{-1}$ and Faradaic efficiency of $\sim 16\%$ vs 0.5 V vs RHE, which is comparatively higher than bulk oxygen vacant TiO_{2-x} and other reported noble metal-based catalyst. The enhanced ENRR activity is predominantly ascribed to the synergistic combination of TiO_{2-x} and COF-Aq to provide enhanced surface activity, lower the work function, and reduced charge transfer barrier. The presence of abundantly exposed active sites on the TiO_{2-x} @COF-Aq facilitates the adsorption of N_2 and other intermediates while the uniquely designed nanostructure expedites the electron transfer from the electrocatalyst surface to the adsorbed intermediates to promote the ENRR activity. Besides ENRR performance, the TiO_{2-x} @COF-Aq demonstrated prolonged electrocatalytic activity up to 60 h of continuous operation without losing any structural and morphological features, providing ample evidence of catalyst longevity

and performance stability. In conclusion, this study not only focuses on the low-cost, nonnoble metal-based electrocatalyst for ENRR but also opens new strategies for the rational designing of advanced material-supported electrocatalysts for high-end electrocatalytic applications.

CRedit authorship contribution statement

B. Mishra: Methodology, Validation, Formal analysis, Investigation, Data curation, Writing – original draft. **S. Biswal:** Methodology, Validation, Formal analysis, Investigation, Data curation, Writing – original draft. **M. Ussama:** Methodology, Validation, Formal analysis, Writing – review & editing. **M. A. Haider:** Resources, Writing – review & editing, Supervision. **BP Tripathi:** Conceptualization, Resources, Writing – review & editing, Supervision, Funding acquisition.

Declaration of Competing Interest

The authors declare that they have no known competing financial interests or personal relationships that could have appeared to influence the work reported in this paper.

Data Availability

Data will be made available on request.

Acknowledgments

BPT is grateful to IIT Delhi for seed grant support. The authors thank IIC, IIT Roorkee, and SAIF, IIT Bombay for XPS and EPR characterizations. We acknowledge the Central Research Facility (CRF) and Nano Research Facility (NRF) for catalyst characterization and High Performance Computing (HPC) facilities of IIT Delhi for computational resources. BM acknowledges the Ph.D. research fellowship from the Ministry of Education, India. SB and MU are grateful to the Ministry of Education, India for the Prime Minister Research Fellowship.

Appendix A. Supporting information

Supplementary data associated with this article can be found in the online version at [doi:10.1016/j.apcatb.2023.123395](https://doi.org/10.1016/j.apcatb.2023.123395).

References

- [1] G. Soloveichik, Electrochemical synthesis of ammonia as a potential alternative to the Haber–Bosch process, *Nat. Catal.* 2 (2019) 377–380, <https://doi.org/10.1038/s41929-019-0280-0>.
- [2] J.W. Erisman, M.A. Sutton, J. Galloway, Z. Klimont, W. Winiwarter, How a century of ammonia synthesis changed the world, *Nat. Geosci.* 1 (2008) 636–639, <https://doi.org/10.1038/ngeo325>.
- [3] S.J. Davis, N.S. Lewis, M. Shaner, S. Aggarwal, D. Arent, I.L. Azevedo, S.M. Benson, T. Bradley, J. Brouwer, Y.-M. Chiang, C.T.M. Clack, A. Cohen, S. Doig, J. Edmonds, P. Fennell, C.B. Field, B. Hannegan, B.-M. Hodge, M.I. Hoffert, E. Ingersoll, P. Jaramillo, K.S. Lackner, K.J. Mach, M. Mastrandrea, J. Ogden, P.F. Peterson, D. L. Sanchez, D. Sperling, J. Stagner, J.E. Trancik, C.-J. Yang, K. Caldeira, Net-zero emissions energy systems, *Science* 360 (2018) eaas9793, <https://doi.org/10.1126/science.aas9793>.
- [4] N. Lazouski, A. Limaye, A. Bose, M.L. Gala, K. Manthiram, D.S. Mallapragada, Cost and performance targets for fully electrochemical ammonia production under flexible operation, *ACS Energy Lett.* 7 (2022) 2627–2633, <https://doi.org/10.1021/acscenergylett.2c01197>.
- [5] R.D. Milton, R. Cai, S. Abdellaoui, D. Leech, A.L. De Lacey, M. Pita, S.D. Minter, Bioelectrochemical haber–bosch process: an ammonia-producing H₂/N₂ Fuel Cell, *Angew. Chem. Int. Ed.* 56 (2017) 2680–2683, <https://doi.org/10.1002/anie.201612500>.
- [6] S.L. Foster, S.I.P. Bakovic, R.D. Duda, S. Maheshwari, R.D. Milton, S.D. Minter, M. J. Janik, J.N. Renner, L.F. Greenlee, Catalysts for nitrogen reduction to ammonia, *Nat. Catal.* 1 (2018) 490–500, <https://doi.org/10.1038/s41929-018-0092-7>.
- [7] C.J.M. van der Ham, M.T.M. Koper, D.G.H. Hetterscheid, Challenges in reduction of dinitrogen by proton and electron transfer, *Chem. Soc. Rev.* 43 (2014) 5183–5191, <https://doi.org/10.1039/C4CS00085D>.
- [8] Y.-C. Hao, Y. Guo, L.-W. Chen, M. Shu, X.-Y. Wang, T.-A. Bu, W.-Y. Gao, N. Zhang, X. Su, X. Feng, J.-W. Zhou, B. Wang, C.-W. Hu, A.-X. Yin, R. Si, Y.-W. Zhang, C.-H. Yan, Promoting nitrogen electroreduction to ammonia with bismuth nanocrystals and potassium cations in water, *Nat. Catal.* 2 (2019) 448–456, <https://doi.org/10.1038/s41929-019-0241-7>.
- [9] M.-M. Shi, D. Bao, B.-R. Wulan, Y.-H. Li, Y.-F. Zhang, J.-M. Yan, Q. Jiang, Au sub-nanoclusters on TiO₂ toward highly efficient and selective electrocatalyst for N₂ conversion to NH₃ at ambient conditions, *Adv. Mater.* 29 (2017), 1606550, <https://doi.org/10.1002/adma.201606550>.
- [10] T. Wu, X. Zhu, Z. Xing, S. Mou, C. Li, Y. Qiao, Q. Liu, Y. Luo, X. Shi, Y. Zhang, X. Sun, Greatly improving electrochemical N₂ reduction over TiO₂ nanoparticles by iron doping, *Angew. Chem. Int. Ed.* 58 (2019) 18449–18453, <https://doi.org/10.1002/anie.201911153>.
- [11] H.Y.F. Sim, J.R.T. Chen, C.S.L. Koh, H.K. Lee, X. Han, G.C. Phan-Quang, J.Y. Pang, C.L. Lay, S. Pedireddy, I.Y. Phang, E.K.L. Yeow, X.Y. Ling, ZIF-induced d-band modification in a bimetallic nanocatalyst: achieving over 44% efficiency in the ambient nitrogen reduction reaction, *Angew. Chem. Int. Ed.* 59 (2020) 16997–17003, <https://doi.org/10.1002/anie.202006071>.
- [12] W. Guo, K. Zhang, Z. Liang, R. Zou, Q. Xu, Electrochemical nitrogen fixation and utilization: theories, advanced catalyst materials and system design, *Chem. Soc. Rev.* 48 (2019) 5658–5716, <https://doi.org/10.1039/C9CS00159J>.
- [13] W. Zhang, J. Low, R. Long, Y. Xiong, Metal-free electrocatalysts for nitrogen reduction reaction, *EnergyChem* 2 (2020), 100040, <https://doi.org/10.1016/j.enchem.2020.100040>.
- [14] Y. Yao, H. Wang, X.-z. Yuan, H. Li, M. Shao, Electrochemical nitrogen reduction reaction on ruthenium, *ACS Energy Lett.* 4 (2019) 1336–1341, <https://doi.org/10.1021/acscenergylett.9b00699>.
- [15] S. Wang, F. Ichihara, H. Pang, H. Chen, J. Ye, Nitrogen fixation reaction derived from nanostructured catalytic materials, *Adv. Funct. Mater.* 28 (2018), 1803309, <https://doi.org/10.1002/adfm.201803309>.
- [16] E. Skúlason, T. Bligaard, S. Gudmundsdóttir, F. Studt, J. Rossmeisl, F. Abild-Pedersen, T. Vegge, H. Jónsson, J.K. Nørskov, A theoretical evaluation of possible transition metal electro-catalysts for N₂ reduction, *Phys. Chem. Chem. Phys.* 14 (2012) 1235–1245, <https://doi.org/10.1039/C1CP22271F>.
- [17] Y. Shi, Y. Liu, Vacancy and N dopants facilitated Ti3+ sites activity in 3D Ti3-xC2Ty MXene for electrochemical nitrogen fixation, *Appl. Catal. B: Environ.* 297 (2021), 120482, <https://doi.org/10.1016/j.apcatb.2021.120482>.
- [18] L. Yang, T. Wu, R. Zhang, H. Zhou, L. Xia, X. Shi, H. Zheng, Y. Zhang, X. Sun, Insights into defective TiO₂ in electrocatalytic N₂ reduction: combining theoretical and experimental studies, *Nanoscale* 11 (2019) 1555–1562, <https://doi.org/10.1039/C8NR09564G>.
- [19] H. Hirakawa, M. Hashimoto, Y. Shiraishi, T. Hirai, Photocatalytic conversion of nitrogen to ammonia with water on surface oxygen vacancies of titanium dioxide, *J. Am. Chem. Soc.* 139 (2017) 10929–10936, <https://doi.org/10.1021/jacs.7b06634>.
- [20] X.-Y. Xie, P. Xiao, W.-H. Fang, G. Cui, W. Thiel, Probing photocatalytic nitrogen reduction to ammonia with water on the rutile TiO₂ (110) surface by first-principles calculations, *ACS Catal.* 9 (2019) 9178–9187, <https://doi.org/10.1021/acscatal.9b01551>.
- [21] S. Cheng, Y.-J. Gao, Y.-L. Yan, X. Gao, S.-H. Zhang, G.-L. Zhuang, S.-W. Deng, Z.-Z. Wei, X. Zhong, J.-G. Wang, Oxygen vacancy enhancing mechanism of nitrogen reduction reaction property in Ru/TiO₂, *J. Energy Chem.* 39 (2019) 144–151, <https://doi.org/10.1016/j.jechem.2019.01.020>.
- [22] Z. Han, C. Choi, S. Hong, T.-S. Wu, Y.-L. Soo, Y. Jung, J. Qiu, Z. Sun, Activated TiO₂ with tuned vacancy for efficient electrochemical nitrogen reduction, *Appl. Catal. B: Environ.* 257 (2019), 117896, <https://doi.org/10.1016/j.apcatb.2019.117896>.
- [23] N. Cao, Z. Chen, K. Zang, J. Xu, J. Zhong, J. Luo, X. Xu, G. Zheng, Doping strain induced bi-Ti3+ pairs for efficient N₂ activation and electrocatalytic fixation, *Nat. Commun.* 10 (2019) 2877, <https://doi.org/10.1038/s41467-019-10888-5>.
- [24] L. Wu, Y. Ji, D. Dai, T. Chen, D. Yang, Y. Liu, Z. Wang, Exceptional size-dependent activity enhancement in the catalytic electroreduction of N₂ over Mo nanoparticles, *Int. J. Hydrog. Energy* 45 (2020) 31841–31848, <https://doi.org/10.1016/j.ijhydene.2020.08.173>.
- [25] L. Hu, H.S. Pillai, C. Feit, K. Shi, Z. Gao, P. Banerjee, H. Xin, X. Feng, Identification of active sites for ammonia electrosynthesis on ruthenium, *ACS Energy Lett.* 7 (2022) 4290–4298, <https://doi.org/10.1021/acscenergylett.2c02175>.
- [26] Y. Wei, F. Zhang, J. Hao, Y. Ling, Y. Gong, S. Wang, J. Wei, Z. Yang, Boosting the photocatalytic performances of covalent organic frameworks enabled by spatial modulation of plasmonic nanocrystals, *Appl. Catal. B: Environ.* 272 (2020), 119035, <https://doi.org/10.1016/j.apcatb.2020.119035>.
- [27] G. Li, H. Jiang, S. Liu, Z. Li, M.G. Kim, Q. Qin, X. Liu, J. Cho, The synergistic effect of Hf–O–Ru bonds and oxygen vacancies in Ru/HfO₂ for enhanced hydrogen evolution, *Nat. Commun.* 13 (2022) 1270, <https://doi.org/10.1038/s41467-022-28947-9>.
- [28] V. Hasija, S. Patil, P. Raizada, A. Aslam Parwaz Khan, A.M. Asiri, Q. Van Le, V.-H. Nguyen, P. Singh, Covalent organic frameworks promoted single metal atom catalysis: strategies and applications, *Coord. Chem. Rev.* 452 (2022), 214298, <https://doi.org/10.1016/j.ccr.2021.214298>.
- [29] T.W. van Deelen, C. Hernández Mejía, K.P. de Jong, Control of metal-support interactions in heterogeneous catalysts to enhance activity and selectivity, *Nat. Catal.* 2 (2019) 955–970, <https://doi.org/10.1038/s41929-019-0364-x>.
- [30] J.H. Chong, M. Sauer, B.O. Patrick, M.J. MacLachlan, Highly stable keto-enamine salicylideneanilines, *Org. Lett.* 5 (2003) 3823–3826. DOI: 10.1021/ol0352714.
- [31] C.R. DeBlase, K.E. Silberstein, T.-T. Truong, H.C. Abrunã, W.R. Dichtel, β -Ketoenamine-linked covalent organic frameworks capable of pseudocapacitive energy storage, *J. Am. Chem. Soc.* 135 (2013) 16821–16824. DOI: 10.1021/ja409421d.

- [32] L. Yang, L. Xu, X. Bai, P. Jin, Enhanced visible-light activation of persulfate by Ti3 + self-doped TiO2/graphene nanocomposite for the rapid and efficient degradation of micropollutants in water, *J. Hazard. Mater.* 365 (2019) 107–117, <https://doi.org/10.1016/j.jhazmat.2018.10.090>.
- [33] J. VandeVondele, M. Krack, F. Mohamed, M. Parrinello, T. Chassaing, J. Hutter, Quickstep: fast and accurate density functional calculations using a mixed Gaussian and plane waves approach, *Comput. Phys. Commun.* 167 (2005) 103–128, <https://doi.org/10.1016/j.cpc.2004.12.014>.
- [34] J. Hutter, M. Iannuzzi, F. Schiffmann, J. VandeVondele, cp2k: atomistic simulations of condensed matter systems, *WIREs Comput. Mol. Sci.* 4 (2014) 15–25. DOI: 10.1002/wcms.1159.
- [35] J.P. Perdew, K. Burke, Y. Wang, Generalized gradient approximation for the exchange-correlation hole of a many-electron system, *Phys. Rev. B* 54 (1996) 16533–16539, <https://doi.org/10.1103/PhysRevB.54.16533>.
- [36] Z. Hu, H. Metiu, Choice of U for DFT+U calculations for titanium oxides, *J. Phys. Chem. C* 115 (2011) 5841–5845, <https://doi.org/10.1021/jp111350u>.
- [37] A. Govind Rajan, M.S. Strano, D. Blankschtein, Ab initio molecular dynamics and lattice dynamics-based force field for modeling hexagonal boron nitride in mechanical and interfacial applications, *J. Phys. Chem. Lett.* 9 (2018) 1584–1591, <https://doi.org/10.1021/acs.jpclett.7b03443>.
- [38] J. VandeVondele, J. Hutter, Gaussian basis sets for accurate calculations on molecular systems in gas and condensed phases, *J. Chem. Phys.* 127 (2007), 114105. DOI: 10.1063/1.2770708.
- [39] S. Grimme, J. Antony, S. Ehrlich, H. Krieg, A consistent and accurate ab initio parametrization of density functional dispersion correction (DFT-D) for the 94 elements H–Pu, *J. Chem. Phys.* 132 (2010), 154104. DOI: 10.1063/1.3382344.
- [40] R. Valero, Á. Morales-García, F. Illas, Theoretical modeling of electronic excitations of gas-phase and solvated TiO2 Nanoclusters and Nanoparticles of Interest in Photocatalysis, *J. Chem. Theory Comput.* 14 (2018) 4391–4404, <https://doi.org/10.1021/acs.jctc.8b00651>.
- [41] C.I. Bayly, P. Cieplak, W. Cornell, P.A. Kollman, A well-behaved electrostatic potential based method using charge restraints for deriving atomic charges: the RESP model, *J. Phys. Chem.* 97 (1993) 10269–10280, <https://doi.org/10.1021/j100142a004>.
- [42] Y. Zhang, Y. Hu, J. Zhao, E. Park, Y. Jin, Q. Liu, W. Zhang, Covalent organic framework-supported Fe–TiO2 nanoparticles as ambient-light-active photocatalysts, *J. Mater. Chem. A* 7 (2019) 16364–16371, <https://doi.org/10.1039/C9TA03649K>.
- [43] A. Khayum M, V. Vijayakumar, S. Karak, S. Kandambeth, M. Bhadra, K. Suresh, N. Acharambath, S. Kurungot, R. Banerjee, Convergent covalent organic framework thin sheets as flexible supercapacitor electrodes, *ACS Appl. Mater. Interfaces* 10 (2018) 28139–28146, <https://doi.org/10.1021/acsami.8b10486>.
- [44] C.R. DeBlase, K.E. Silberstein, T.-T. Truong, H.D. Abruña, W.R. Dichtel, β -ketoenamine-linked covalent organic frameworks capable of pseudocapacitive energy storage, *J. Am. Chem. Soc.* 135 (2013) 16821–16824. DOI: 10.1021/ja409421d.
- [45] S. He, T. Zeng, S. Wang, H. Niu, Y. Cai, Facile synthesis of magnetic covalent organic framework with three-dimensional bouquet-like structure for enhanced extraction of organic targets, *ACS Appl. Mater. Interfaces* 9 (2017) 2959–2965, <https://doi.org/10.1021/acsami.6b13643>.
- [46] Q. Li, X. Lan, G. An, L. Ricardez-Sandoval, Z. Wang, G. Bai, Visible-light-responsive anthraquinone functionalized covalent organic frameworks for metal-free selective oxidation of sulfides: effects of morphology and structure, *ACS Catal.* 10 (2020) 6664–6675, <https://doi.org/10.1021/acscatal.0c00290>.
- [47] H. Salemi, M. Debruyne, V. Van Speybroeck, P. Van Der Voort, M. D’Hooghe, C. V. Stevens, Covalent organic framework supported palladium catalysts, *J. Mater. Chem. A* 10 (2022) 20707–20729, <https://doi.org/10.1039/D2TA05234B>.
- [48] S. Li, Y. Yang, L. Liu, Q. Zhao, Electron transfer-induced catalytic enhancement over bismuth nanoparticles supported by N-doped graphene, *Chem. Eng. J.* 334 (2018) 1691–1698, <https://doi.org/10.1016/j.cej.2017.11.127>.
- [49] W. Hu, Y. Liu, R.L. Withers, T.J. Frankcombe, L. Norén, A. Snashall, M. Kitchin, P. Smith, B. Gong, H. Chen, J. Schiemer, F. Brink, J. Wong-Leung, Electron-pinned defect-dipoles for high-performance colossal permittivity materials, *Nat. Mater.* 12 (2013) 821–826, <https://doi.org/10.1038/nmat3691>.
- [50] G. Ou, Y. Xu, B. Wen, R. Lin, B. Ge, Y. Tang, Y. Liang, C. Yang, K. Huang, D. Zu, R. Yu, W. Chen, J. Li, H. Wu, L.-M. Liu, Y. Li, Tuning defects in oxides at room temperature by lithium reduction, *Nat. Commun.* 9 (2018) 1302, <https://doi.org/10.1038/s41467-018-03765-0>.
- [51] X. Tong, X. Zhan, Z. Gao, G. Zhang, Y. Xie, J. Tian, H. Ranganathan, D. Li, J. P. Claverie, S. Sun, Effect of the metal–support interaction in platinum anchoring on heteroatom-doped graphene for enhanced oxygen reduction reaction, *Chem. Commun.* 58 (2022) 11519–11522, <https://doi.org/10.1039/D2CC03505G>.
- [52] Y. Zhang, Z. Xu, G. Li, X. Huang, W. Hao, Y. Bi, Direct observation of oxygen vacancy self-healing on TiO2 photocatalysts for solar water splitting, *Angew. Chem. Int. Ed.* 58 (2019) 14229–14233, <https://doi.org/10.1002/anie.201907954>.
- [53] R. K. P. N., V. C.P. T.S. Khan, S. Gupta, M.A. Haider, D. Jagadeesan, CuO as a reactive and reusable reagent for the hydrogenation of nitroarenes, *Appl. Catal. B: Environ.* 297 (2021), 120417, <https://doi.org/10.1016/j.apcatb.2021.120417>.
- [54] C. Fang, T. Bi, X. Xu, N. Yu, Z. Cui, R. Jiang, B. Geng, Oxygen vacancy-enhanced electrocatalytic performances of TiO2 nanosheets toward N2 reduction reaction, *Adv. Mater. Interfaces* 6 (2019), 1901034, <https://doi.org/10.1002/admi.201901034>.
- [55] H. Li, Y. Guo, J. Robertson, Calculation of TiO2 surface and subsurface oxygen vacancy by the screened exchange functional, *J. Phys. Chem. C* 119 (2015) 18160–18166, <https://doi.org/10.1021/acs.jpcc.5b02430>.
- [56] W. Li, K. Li, Y. Ye, S. Zhang, Y. Liu, G. Wang, C. Liang, H. Zhang, H. Zhao, Efficient electrocatalytic nitrogen reduction to ammonia with aqueous silver nanodots, *Commun. Chem.* 4 (2021) 10, <https://doi.org/10.1038/s42004-021-00449-7>.
- [57] J. Wang, L. Yu, L. Hu, G. Chen, H. Xin, X. Feng, Ambient ammonia synthesis via palladium-catalyzed electrohydrogenation of dinitrogen at low overpotential, *Nat. Commun.* 9 (2018) 1795, <https://doi.org/10.1038/s41467-018-04213-9>.
- [58] B. Yu, H. Li, J. White, S. Donne, J. Yi, S. Xi, Y. Fu, G. Henkelman, H. Yu, Z. Chen, T. Ma, Tuning the catalytic preference of ruthenium catalysts for nitrogen reduction by atomic dispersion, *Adv. Funct. Mater.* 30 (2020), 1905665, <https://doi.org/10.1002/adfm.201905665>.
- [59] X. Zhang, R.-M. Kong, H. Du, L. Xia, F. Qu, Highly efficient electrochemical ammonia synthesis via nitrogen reduction reactions on a VN nanowire array under ambient conditions, *Chem. Commun.* 54 (2018) 5323–5325, <https://doi.org/10.1039/C8CC00459E>.
- [60] H. Liu, X. Wu, J. Xu, Microfluidic tailoring of a ru nanodots/carbon heterocatalyst for electrocatalytic nitrogen fixation, *ACS Appl. Nano Mater.* 6 (2023) 12282–12291, <https://doi.org/10.1021/acsnano.3c01966>.
- [61] J. Chen, W. Zhang, H. Li, W. Li, D. Zhao, Recent advances in TiO2-based catalysts for N2 reduction reaction, *SusMat* 1 (2021) 174–193. DOI: 10.1002/sus2.13.
- [62] J. Yang, Y. Guo, R. Jiang, F. Qin, H. Zhang, W. Lu, J. Wang, J.C. Yu, High-efficiency “working-in-tandem” nitrogen photofixation achieved by assembling plasmonic gold nanocrystals on ultrathin titania nanosheets, *J. Am. Chem. Soc.* 140 (2018) 8497–8508, <https://doi.org/10.1021/jacs.8b03537>.
- [63] W.P. Utomo, H. Wu, Y.H. Ng, Modulating the active sites of oxygen-deficient TiO2 by copper loading for enhanced electrocatalytic nitrogen reduction to ammonia, *Small* 18 (2022), 2200996, <https://doi.org/10.1002/smll.202200996>.
- [64] Y. Guo, T. Wang, Q. Yang, X. Li, H. Li, Y. Wang, T. Jiao, Z. Huang, B. Dong, W. Zhang, J. Fan, C. Zhi, Highly efficient electrochemical reduction of nitrogen to ammonia on surface termination modified Ti3C2Tx MXene nanosheets, *ACS Nano* 14 (2020) 9089–9097, <https://doi.org/10.1021/acsnano.0c04284>.
- [65] J.Y. Cheon, J.H. Kim, J.H. Kim, K.C. Goddeti, J.Y. Park, S.H. Joo, Intrinsic relationship between enhanced oxygen reduction reaction activity and nanoscale work function of doped carbons, *J. Am. Chem. Soc.* 136 (2014) 8875–8878. DOI: 10.1021/ja503557x.
- [66] S. Zhao, X. Lu, L. Wang, J. Gale, R. Amal, Carbon-based metal-free catalysts for electrocatalytic reduction of nitrogen for synthesis of ammonia at ambient conditions, *Adv. Mater.* 31 (2019), 1805367, <https://doi.org/10.1002/adma.201805367>.
- [67] P. Song, H. Wang, L. Kang, B. Ran, H. Song, R. Wang, Electrochemical nitrogen reduction to ammonia at ambient conditions on nitrogen and phosphorus co-doped porous carbon, *Chem. Commun.* 55 (2019) 687–690, <https://doi.org/10.1039/C8CC09256G>.
- [68] J. Mu, X.-W. Gao, Z. Liu, W.-B. Luo, Z. Sun, Q. Gu, F. Li, Boosting nitrogen electrocatalytic fixation by three-dimensional TiO2–8N6 nanowire arrays, *J. Energy Chem.* 75 (2022) 293–300, <https://doi.org/10.1016/j.jechem.2022.08.007>.